



4-2017

## Clinical Applications of Near-Infrared Diffuse Correlation Spectroscopy and Tomography for Tissue Blood Flow Monitoring and Imaging

Yu Shang

*North University of China, China*

Ting Li

*University of Electronic Science & Technology of China, China*

Guoqiang Yu

*University of Kentucky, gyu2@uky.edu*

Follow this and additional works at: [https://uknowledge.uky.edu/cbme\\_facpub](https://uknowledge.uky.edu/cbme_facpub)



Part of the [Biomedical Engineering and Bioengineering Commons](#), and the [Physiology Commons](#)

**Right click to open a feedback form in a new tab to let us know how this document benefits you.**

---

### Repository Citation

Shang, Yu; Li, Ting; and Yu, Guoqiang, "Clinical Applications of Near-Infrared Diffuse Correlation Spectroscopy and Tomography for Tissue Blood Flow Monitoring and Imaging" (2017). *Biomedical Engineering Faculty Publications*. 38.

[https://uknowledge.uky.edu/cbme\\_facpub/38](https://uknowledge.uky.edu/cbme_facpub/38)

This Review is brought to you for free and open access by the Biomedical Engineering at UKnowledge. It has been accepted for inclusion in Biomedical Engineering Faculty Publications by an authorized administrator of UKnowledge. For more information, please contact [UKnowledge@lsv.uky.edu](mailto:UKnowledge@lsv.uky.edu).

---

# Clinical Applications of Near-Infrared Diffuse Correlation Spectroscopy and Tomography for Tissue Blood Flow Monitoring and Imaging

Digital Object Identifier (DOI)

<https://doi.org/10.1088/1361-6579/aa60b7>

## Notes/Citation Information

Published in *Physiological Measurement*, v. 38, no. 4, p. R1-R26.

© 2017 Institute of Physics and Engineering in Medicine

After a 12-month embargo period from the publication of the Version of Record of this article, everyone is permitted to use, copy, and redistribute this article for non-commercial purposes only, provided that they adhere to all the terms of the Creative Commons Attribution-NonCommercial-NoDerivs 3.0 Unported license: <https://creativecommons.org/licences/by-nc-nd/3.0>

The document available for download is the authors' post-peer-review final draft of the article.

## TOPICAL REVIEW

# Clinical applications of near-infrared diffuse correlation spectroscopy and tomography for tissue blood flow monitoring and imaging

To cite this article: Yu Shang *et al* 2017 *Physiol. Meas.* **38** R1

## Manuscript version: Accepted Manuscript

Accepted Manuscript is “the version of the article accepted for publication including all changes made as a result of the peer review process, and which may also include the addition to the article by IOP Publishing of a header, an article ID, a cover sheet and/or an ‘Accepted Manuscript’ watermark, but excluding any other editing, typesetting or other changes made by IOP Publishing and/or its licensors”

This Accepted Manuscript is © © 2017 Institute of Physics and Engineering in Medicine.

During the embargo period (the 12 month period from the publication of the Version of Record of this article), the Accepted Manuscript is fully protected by copyright and cannot be reused or reposted elsewhere.

As the Version of Record of this article is going to be / has been published on a subscription basis, this Accepted Manuscript is available for reuse under a CC BY-NC-ND 3.0 licence after the 12 month embargo period.

After the embargo period, everyone is permitted to use copy and redistribute this article for non-commercial purposes only, provided that they adhere to all the terms of the licence <https://creativecommons.org/licenses/by-nc-nd/3.0>

Although reasonable endeavours have been taken to obtain all necessary permissions from third parties to include their copyrighted content within this article, their full citation and copyright line may not be present in this Accepted Manuscript version. Before using any content from this article, please refer to the Version of Record on IOPscience once published for full citation and copyright details, as permissions will likely be required. All third party content is fully copyright protected, unless specifically stated otherwise in the figure caption in the Version of Record.

View the [article online](#) for updates and enhancements.

1  
2  
3  
4 **Clinical Applications of Near-infrared Diffuse Correlation Spectroscopy and**  
5  
6  
7 **Tomography for Tissue Blood Flow Monitoring and Imaging**  
8  
9

10  
11 Yu Shang<sup>1</sup>, Ting Li<sup>2</sup>, and Guoqiang Yu<sup>3,\*</sup>  
12  
13

14  
15  
16  
17 <sup>1</sup>Key Laboratory of Instrumentation Science & Dynamic Measurement  
18

19  
20 North University of China  
21

22  
23 No.3 Xueyuan Road  
24

25  
26 Taiyuan, Shanxi 030051, China  
27

28  
29 E-mail: [yushang@nuc.edu.cn](mailto:yushang@nuc.edu.cn)  
30  
31  
32

33  
34 <sup>2</sup>State Key Lab Elect Thin Film & Integrated Device, University of Electronic Science &  
35

36  
37 Technology of China  
38

39  
40 Chengdu, Sichuan 610054, China  
41

42  
43 E-mail: [liting@uestc.edu.cn](mailto:liting@uestc.edu.cn)  
44  
45

46  
47 <sup>3</sup>Department of Biomedical Engineering  
48

49  
50 University of Kentucky  
51

52  
53 514C RMB, 143 Graham Avenue  
54

55  
56 Lexington, KY 40506-0108, USA  
57

58  
59 \*E-mail: [guoqiang.yu@uky.edu](mailto:guoqiang.yu@uky.edu)  
60

**Abstract**

Blood flow is one such available observable promoting a wealth of physiological insight both individually and in combination with other metrics. Near-infrared diffuse correlation spectroscopy (DCS) and, to a lesser extent, diffuse correlation tomography (DCT), have increasingly received interest over the past decade as noninvasive methods for tissue blood flow measurements and imaging. DCS/DCT offers several attractive features for tissue blood flow measurements/imaging such as noninvasiveness, portability, high temporal resolution, and relatively large penetration depth (up to several centimeters). This review first introduces the basic principle and instrumentation of DCS/DCT, followed by presenting clinical application examples of DCS/DCT for the diagnosis and therapeutic monitoring of diseases in a variety of organs/tissues including brain, skeletal muscle, and tumor. Clinical study results demonstrate technical versatility of DCS/DCT in providing important information for disease diagnosis and intervention monitoring.

## Table of Contents

1		
2		
3		
4		
5		
6		
7	1. Introduction	4
8		
9	2. DCS/DCT Methods	6
10		
11	2.1 Diffuse Correlation Spectroscopy (DCS)	6
12		
13	2.2 Diffuse Correlation Tomography (DCT)	9
14		
15	2.3 DCS/DCT Instrumentation	11
16		
17	3. Clinical Application Examples	12
18		
19	3.1 Brain	13
20		
21	3.1.1 Diagnosis of cardio-cerebral diseases	13
22		
23	3.1.2 Therapeutic monitoring of cardio-cerebral diseases	17
24		
25	3.2 Skeletal muscle	19
26		
27	3.2.1 Diagnosis of muscular diseases	19
28		
29	3.2.2 Therapeutic monitoring of muscular diseases	21
30		
31	3.3 Tumor	22
32		
33	3.3.1 Diagnosis of tumors	22
34		
35	3.3.2 Therapeutic monitoring of tumor treatments	24
36		
37	4. Summary and future perspectives	26
38		
39	Acknowledgments	30
40		
41	References	31
42		
43		
44		
45		
46		
47		
48		
49		
50		
51		
52		
53		
54		
55		
56		
57		
58		
59		
60		

## 1. Introduction

Near-infrared (NIR) diffuse optical technologies have gained popularity in recent years as simple, fast, continuous, portable, and relatively inexpensive methods for noninvasive quantification of hemodynamics and metabolism in deep tissues up to several centimeters (Vardi and Nini, 2008; Schachner *et al.*, 2008; Bouye *et al.*, 2005; Boas *et al.*, 2001; Ferrari *et al.*, 2011; Jobsis, 1977; Murkin and Arango, 2009; Shuler *et al.*, 2009). One type of NIR technology, namely near-infrared spectroscopy (NIRS) or diffuse optical spectroscopy (DOS), takes advantage of the low absorption spectrum of biological tissues in the NIR range (650-950 nm) and penetrates deep tissues to detect light absorption by oxy-hemoglobin ( $\text{HbO}_2$ ) and deoxy-hemoglobin (Hb) in red blood cells (RBCs) (Kim *et al.*, 2005; Strangman *et al.*, 2003). As a result, oxy-, deoxy-, total- hemoglobin concentrations (i.e.,  $[\text{HbO}_2]$ ,  $[\text{Hb}]$ , and THC) and tissue blood oxygen saturation ( $\text{StO}_2$ ) in local tissue microvasculature can be quantified (Liu *et al.*, 1995; Boas *et al.*, 2001; Wolf *et al.*, 2003; Fantini *et al.*, 1995). Over past decades, a variety of NIRS/DOS technologies have been extensively explored to study various diseases affecting blood oxygenation levels in local and regional tissues (Liu *et al.*, 1995; Wolf *et al.*, 2003; Quaresima *et al.*, 2004; Fantini *et al.*, 1995; Patterson *et al.*, 1989; Al-Rawi and Kirkpatrick, 2006). Correspondingly, diffuse optical tomography (DOT) based on NIRS/DOS has also been developed for 3-dimensional (3-D) imaging of oxygenation distributions in organs or regional tissues (Intes *et al.*, 2010; Eggebrecht *et al.*, 2014; Deghani *et al.*, 2009; Zhang *et al.*, 2013; Arridge and Hebden, 1997; Jermyn *et al.*, 2013).

Another emerging NIR technology, diffuse correlation spectroscopy (DCS), has also been developed to directly measure blood flow variations in deep tissue microvasculature (Boas *et*

1  
2  
3  
4 *al.*, 1995; Maret and Wolf, 1989; Pine *et al.*, 1988; Yu *et al.*, 2005a; Jaillon *et al.*, 2007; Boas,  
5  
6  
7 1996; Durduran, 2004; Choe, 2005; Zhou, 2007; Irwin, 2011; Gurley, 2012; Cheng, 2013; He,  
8  
9  
10 2015; Dong, 2015). DCS uses *coherent* NIR light to penetrate deep tissues and monitors  
11  
12 temporal light intensity fluctuation caused by moving scatterers (primarily RBCs in the  
13  
14 microvasculature) to extract a blood flow index (BFI) (Irwin *et al.*, 2011; Cheung *et al.*, 2001).  
15  
16  
17 The relative change of blood flow (rBF) is calculated by normalizing BFI to its baseline value  
18  
19 before the physiological change occurs. DCS measurements of tissue blood flow changes  
20  
21 have been extensively validated against other standards, including power spectral Doppler  
22  
23 ultrasound (Yu *et al.*, 2005b), Doppler ultrasound (Buckley *et al.*, 2009; Roche-Labarbe *et al.*,  
24  
25 2010), laser Doppler (Durduran, 2004; Shang *et al.*, 2011a), Xenon computed tomography  
26  
27 (Xenon-CT) (Kim *et al.*, 2010), fluorescent microsphere flow measurement (Zhou *et al.*,  
28  
29 2009), and arterial spin labeling magnetic resonance imaging (ASL-MRI) (Yu *et al.*, 2007). In  
30  
31 some studies, DCS has been combined with NIRS/DOS in hybrid instruments to  
32  
33 simultaneously measure tissue blood flow and oxygenation (Durduran *et al.*, 2004; Yu *et al.*,  
34  
35 2005a; Cheng *et al.*, 2012; Munk *et al.*, 2012; Shang *et al.*, 2012; Gurley *et al.*, 2012), which  
36  
37 allows for the derivation of metabolic rate of tissue oxygen consumption.  
38  
39  
40  
41  
42  
43  
44  
45  
46

47 Despite advances in DCS applicability, there have been limited tomographic imaging  
48  
49 realizations. An early contact-measurement based 3-D diffuse correlation tomography (DCT)  
50  
51 approach using an optical fiber array was applied to tissue phantoms with a semi-infinite  
52  
53 geometry (Boas and Yodh, 1997), but is disadvantaged *in vivo* due to the irregular geometries  
54  
55 of biological tissues. A few noncontact-measurement based DCT examinations have been  
56  
57 recently conducted to avoid tissue hemodynamic variations induced by the probe compression  
58  
59  
60



1  
2  
3  
4 or the disturbance of sensitive tissue areas (Culver *et al.*, 2003; Huang *et al.*, 2015a; Zhou *et*  
5  
6  
7 *al.*, 2006; Lin *et al.*, 2014; He *et al.*, 2015; Huang *et al.*, 2015b). In these noncontact  
8  
9  
10 measurement systems, lenses were positioned between a sample and an optical fiber array  
11  
12 connected to the light sources and detection elements. The noncontact DCS/DCT has been  
13  
14  
15 successfully applied in examining blood flow distributions in animal models (Zhou *et al.*,  
16  
17  
18 2006; Culver *et al.*, 2003) and human subjects (Li *et al.*, 2013; He *et al.*, 2015; Lin *et al.*,  
19  
20  
21 2012; Huang *et al.*, 2015c; Huang *et al.*, 2015b).

22  
23 Since NIRS/DOS/DOT technologies for tissue blood oxygenation measurements have  
24  
25  
26 been broadly reviewed (Durduran *et al.*, 2010a; Ferrari *et al.*, 2011; Ghosh *et al.*, 2012; Wolf  
27  
28  
29 *et al.*, 2007), our review focuses on the DCS/DCT technologies for tissue blood flow  
30  
31  
32 measurements in the clinic. We first introduce the principle and instrumentation of DCS/DCT.  
33  
34 We then provide typical clinical examples of DCS/DCT for the diagnosis of diseases and  
35  
36  
37 therapeutic monitoring of interventions in a variety of organs/tissues such as brain, skeletal  
38  
39  
40 muscle, and tumor. Finally, we highlight the limitations of DCS/DCT and point out future  
41  
42  
43 perspectives in technology development and clinical applications.

## 44 45 **2. DCS/DCT Methods**

### 46 47 48 **2.1 Diffuse Correlation Spectroscopy (DCS)**

49  
50  
51 DCS originates from the concept of “dynamic light scattering (DLS)”, a technology that  
52  
53  
54 can be used to quantify the motion of moving scatterers in a thin solution through  
55  
56  
57 investigating the correlation of light electric field after photons are scattered once by the  
58  
59  
60 moving scatterers (i.e., single light scattering) (Brown, 1993; Fletcher, 1976). The extension  
from single light scattering to multiple light scattering has been explored since 1980s (Maret

1  
2  
3  
4 and Wolf, 1987; Pine *et al.*, 1988; Boas *et al.*, 1995). This extension, called diffusing-wave  
5  
6 spectroscopy (DWS) (Pine *et al.*, 1988; Li *et al.*, 2005; Jaillon *et al.*, 2006) or diffuse  
7  
8 correlation spectroscopy (DCS) (Cheung *et al.*, 2001; Yu *et al.*, 2005a; Gagnon *et al.*, 2008;  
9  
10 Boas and Yodh, 1997; Boas *et al.*, 1995), makes it possible to quantify the motion of moving  
11  
12 scatterers in a thick sample, such as red blood cells (RBCs) flowing through biological  
13  
14 tissues.  
15  
16  
17  
18  
19

20 The principle and instrumentation of DCS have been described elsewhere (Boas *et al.*,  
21  
22 1995; Cheung *et al.*, 2001; Durduran and Yodh, 2014; Irwin *et al.*, 2011; Yu, 2012b, a; Yu,  
23  
24 2012c). Briefly, a long-coherence laser delivers NIR light via an optical fiber to the tissue  
25  
26 (**Fig. 1a**). Photons entering into the tissue are either absorbed or more dominantly, scattered  
27  
28 by static scatterers (e.g., organelles and mitochondria) and dynamic scatterers (mainly moving  
29  
30 RBCs). Due to the scattering effect photons may change directions many times while  
31  
32 traveling throughout the tissue, resulting in light diffusion. Only a few photons can eventually  
33  
34 reach tissue surface and be collected by a single-mode detector fiber placed millimeters or  
35  
36 centimeters away from the source fiber. Photons collected by the detector fiber are detected  
37  
38 by a single photon-counting avalanche photodiode (APD) to yield light intensity signals (**Fig.**  
39  
40 **1b**).  
41  
42  
43  
44  
45  
46  
47  
48

49 The detected light intensity fluctuates with time (**Fig. 1b**), which is caused by the motion  
50  
51 of moving scatterers (mainly RBCs) inside the tissue volume measured. To quantify the  
52  
53 motion of RBCs (i.e., blood flow) the normalized light intensity temporal autocorrelation  
54  
55 function ( $g_2(\tau)$ ) is calculated by a hardware correlator board or a software correlator, which  
56  
57 can then be converted to the normalized electric field temporal autocorrelation function ( $g_1(\tau)$ ),  
58  
59  
60

**Fig. 1c)** through the Siegert relation (Rice, 1954):

$$g_2(\vec{r}, \tau) = 1 + \beta |g_1(\vec{r}, \tau)|^2 \quad (1)$$

where  $\tau$  is the correlation delay time,  $\vec{r}$  is the position vector, and  $\beta$  is a parameter which is dependent of laser stability, coherence length, and the number of speckles detected.

The  $g_1(\tau)$  can be expressed in an integral form (Boas and Yodh, 1997; Li *et al.*, 2013; Pine *et al.*, 1988; Maret and Wolf, 1987)

$$g_1(\tau) = \frac{\langle E(0)E^*(\tau) \rangle}{\langle |E(0)|^2 \rangle} = \int_0^\infty P(s) \exp(-\frac{1}{3}k_0^2 \langle \Delta r^2(\tau) \rangle \frac{s}{l^*}) ds \quad (2)$$

Here  $E(0)$  and  $E^*(\tau)$  are the scattered light electric field at time 0 and its conjugation at time  $\tau$ , respectively.  $P(s)$  is the normalized distribution of detected photon path length  $s$ ,  $k_0$  is the wave vector magnitude of the light in the medium, and  $l^*$  is the photon random-walk step length, which is equal to  $1/\mu_s'$  ( $\mu_s'$  is the medium reduced scattering coefficient).

The unknown  $\langle \Delta r^2(\tau) \rangle$  represents the mean-square-displacement of moving scatterers, which is conventionally difficult to be solved directly using **Eq. 2**. Alternately, the integral form of autocorrelation function can be converted to a partial differential equation form (Pine *et al.*, 1990). As such, the unnormalized electric field autocorrelation function  $G_1(\tau) = \langle E(0)E^*(\tau) \rangle$  satisfies a correlation diffusion equation (Cheung *et al.*, 2001; Boas and Yodh, 1997)

$$\left( D\nabla^2 - \nu\mu_a - \frac{1}{3}\nu\mu_s'k_0^2 \langle \Delta r^2(\tau) \rangle \right) G_1(\vec{r}, \tau) = -\nu S(\vec{r}) \quad (3)$$

Here,  $\nu$  is the light speed in the medium;  $\mu_a$  is the medium absorption coefficient;  $D \approx \nu/3\mu_s'$  is the medium photon diffusion coefficient, and  $S(\vec{r})$  is the continuous-wave

1  
2  
3  
4 isotropic source. The form of  $\langle \Delta r^2(\tau) \rangle$  depends on a flow model specifically adopted. For  
5  
6  
7 example, a diffuse model, i.e.,  $\langle \Delta r^2(\tau) \rangle = 6D_B\tau$ , has been found to fit experimental data well  
8  
9  
10 over a wide range of different tissues (Cheung *et al.*, 2001; Irwin *et al.*, 2011). Here,  $D_B$  is the  
11  
12 effective diffusive coefficient. To account for the fact that not all scatterers are “moving” in  
13  
14 the tissue, a factor  $\alpha$ , representing the ratio of “moving” scatterers to the total number of  
15  
16 scatterers, is added to  $\langle \Delta r^2(\tau) \rangle$  (i.e.,  $\langle \Delta r^2(\tau) \rangle = 6\alpha D_B\tau$ ). The combined term,  $\alpha D_B$ , is referred  
17  
18 to as blood flow index (BFI) in biological tissues. The  $\alpha D_B$  can be extracted by fitting the  
19  
20 measured autocorrelation function curve to an analytical solution of the correlation diffusion  
21  
22 equation (Eq. 3) under certain geometries (e.g., semi-infinite boundary) (Cheung *et al.*, 2001;  
23  
24 Dong *et al.*, 2012a; Roche-Labarbe *et al.*, 2010; Irwin *et al.*, 2011).

## 2.2 Diffuse Correlation Tomography (DCT)

25  
26  
27  
28  
29  
30  
31  
32  
33 The extension of DCS to DCT is comparable to that of DOS extension to DOT, which  
34  
35 images the optical property distribution based on photon diffusion equation and its inverse  
36  
37 solutions (i.e., image reconstruction). A DOT instrument typically illuminates tissue and  
38  
39 measures the diffusive light leaving the tissue with multiple sources and detectors on the  
40  
41 tissue boundary (Intes *et al.*, 2010; Eggebrecht *et al.*, 2014; Dehghani *et al.*, 2009; Zhang *et al.*,  
42  
43 2013). The diffusive propagation of light in tissue can be characterized with photon  
44  
45 diffuse equation and parameterized in terms of the unknown  $\mu_a(\vec{r})$  and  $\mu'_s(\vec{r})$  at different  
46  
47 locations ( $\vec{r}$ ) of the measured tissue volume. One can then “invert” the propagation model to  
48  
49 recover these unknown parameters. Imaging with DOT has been described in many papers  
50  
51 covering computer simulations, phantom tests, and *in vivo* applications (Franceschini *et al.*,  
52  
53 2006; Durduran *et al.*, 2010a; Eggebrecht *et al.*, 2014; Arridge and Lionheart, 1998; Arridge  
54  
55  
56  
57  
58  
59  
60

and Hebden, 1997; Jermyn *et al.*, 2013; Dehghani *et al.*, 2009).

Similarly, DCT requires a large number of sources and detectors to measure autocorrelation functions on the tissue boundary. Early DCT approaches rely on analytical solutions of **Eq. 3** with the assumption of simple semi-infinite geometries and/or strict heterogeneities (e.g., spherical anomaly) of tissues (Zhou *et al.*, 2006; Culver *et al.*, 2003), which precludes the transition to complex boundaries and imperfect heterogeneities in realistic tissues.

The finite-element-method (FEM) framework has been applied to model light transport in highly diffuse media to resolve the geometry and heterogeneity limitations for DOS/DOT (Arridge and Lionheart, 1998; Arridge and Hebden, 1997; Eggebrecht *et al.*, 2014; Dehghani *et al.*, 2009; Jermyn *et al.*, 2013). For example, NIRFAST ([www.nirfast.org](http://www.nirfast.org)) (Dehghani *et al.*, 2009; Jermyn *et al.*, 2013) and TOAST++ (<http://web4.cs.ucl.ac.uk/research/vis/toast/>) (Schweiger and Arridge, 2014) are publically available image reconstruction toolboxes based on the diffusive model and FEM for DOT

Exploiting the high mathematical similarity of the forward and inverse problems (e.g., boundary conditions and mathematical assumptions) between DOT and DCT, our group first reported the application of FEM in DCT (Lin *et al.*, 2014; Huang *et al.*, 2015a; He *et al.*, 2015; Huang *et al.*, 2015b). We introduced this concept into the FEM-based light transport and image reconstruction modules in NIRFAST (Dehghani *et al.*, 2009), as a shortcut for FEM implementation of DCT. Specifically, we used the “effective  $\mu_a(\vec{r})$ ” (i.e.,  $\mu_a(\vec{r}) + 2\mu_s'(\vec{r})k_0^2\Delta\alpha D_b(\vec{r})\tau$ ) and measured  $G_1(\vec{r}, \tau)$  to replace the  $\mu_a(\vec{r})$  and photon fluence rate  $\Phi(\vec{r}, t)$  respectively in the NIRFAST for the accomplishment of DCT in tissues

1  
2  
3  
4 with complex boundaries (Lin *et al.*, 2014; Huang *et al.*, 2015a; He *et al.*, 2015; Huang *et al.*,  
5  
6  
7 2015b). Computer simulations, phantom tests, and *in-vivo* studies have verified the accuracy  
8  
9  
10 of our modifications of NIRFAST adapted for DCT. As a result, the realm of DCT becomes  
11  
12 available for comprehensive imaging under complex geometries and heterogeneous optical  
13  
14  
15 properties.

### 17 **2.3 DCS/DCT Instrumentation**

18  
19  
20 Typical DCS/DCT systems are illustrated in **Fig. 2**. The DCS/DCT systems consist of  
21  
22 long-coherence NIR lasers (e.g., 785 nm, Crystalaser, USA), single photon-counting APDs  
23  
24 (e.g., SPCM-AQR-12, Perkin Elmer Inc., Canada), and digital correlator boards (e.g.,  
25  
26 FLEX03LQ, www.correlator.com, USA). A control panel (laptop or desktop) is used to  
27  
28 control the DCS/DCT system for data collection and calculation of temporal autocorrelation  
29  
30  
31 function via the correlator board. Blood flow index ( $\alpha D_B$ ) can be extracted by fitting the  
32  
33 measured autocorrelation function curve to an analytical solution of **Eq. 3** under certain  
34  
35 geometries. In contrast to the portable DCS device (**b**) with a limited number of sources and  
36  
37 detectors, the DCT instrument (**c**) has a large number of sources and detectors for 3-D flow  
38  
39  
40  
41  
42 imaging.

43  
44  
45  
46  
47 A variety of fiber-optics probes have been designed for DCS (**Fig. 3**) and DCT (**Fig. 4**)  
48  
49 measurements in different applications (Huang *et al.*, 2015c; Durduran *et al.*, 2005; Yu *et al.*,  
50  
51 2011; Shang *et al.*, 2011b; Huang *et al.*, 2015b) (see **Section 3**). These probes are connected  
52  
53 to the DCS/DCT instruments (**Fig. 2**) through optical fibers for light delivery and detection.  
54  
55  
56  
57 Examples of DCS probes for the studies of brains, skeletal muscles, and tumors are illustrated  
58  
59 in **Fig. 3a-e**, respectively. For instance, a hand-held probe was designed to scan over a breast  
60

1  
2  
3  
4 tumor in both horizontal and vertical directions for diagnostic purpose (Durduran *et al.*, 2005)  
5  
6  
7 (**Fig. 3d**). For the tissues whose shapes promote hemodynamic variations induced by  
8  
9  
10 compression or disturb sensitive areas, DCS probes were designed in a noncontact manner  
11  
12 (Huang *et al.*, 2015c) (**Fig. 3f**). In the noncontact measurement design, a lens system with  
13  
14 separated source and detector paths was utilized to focus the light from the source and  
15  
16 detector fibers on the measured tissue surface. The noncontact DCS (ncDCS) probe was also  
17  
18 extended to a noncontact imaging probe head for DCT measurements, which consisted of a  
19  
20 linear array of 15 photodetectors and two laser sources connected to a mobile lens-focusing  
21  
22 system (**Fig. 4**) (Lin *et al.*, 2014; He *et al.*, 2015; Huang *et al.*, 2015b). A motorized stage was  
23  
24 utilized for automatic scanning (**Fig. 4a**), enabling large ROI coverage and flexible S-D  
25  
26 arrangements without greatly increasing hardware requirements and costs. This new design of  
27  
28 noncontact DCT (ncDCT) probe, combined with a novel FEM framework for DCT image  
29  
30 reconstruction, has been validated in a tissue-like phantom with anomaly flow contrast design  
31  
32 (**Fig. 4d**) (Lin *et al.*, 2014) and has been applied in detection of breast tumors (He *et al.*, 2015;  
33  
34 Huang *et al.*, 2015b). In practice, any innovations adopted in DOS/DOT probes can be  
35  
36 adapted for the design of DCS/DCT probes, and a combined probe integrating DOS/DOT and  
37  
38 DCS/DCT measurements can be constructed by adding extra optical fibers.  
39  
40  
41  
42  
43  
44  
45  
46  
47  
48  
49

### 50 **3. Clinical Application Examples**

51  
52 DCS/DCT technologies have been extensively explored to be used in animal models and  
53  
54 human subjects for the diagnosis and therapeutic monitoring of diseases in various tissues and  
55  
56 organs including brains (Cheng *et al.*, 2014; Hou *et al.*, 2014; Busch *et al.*, 2016a; Kim *et al.*,  
57  
58 2014; Kim *et al.*, 2010; Favilla *et al.*, 2014; Lin *et al.*, 2016; Dehaes *et al.*, 2014; Durduran *et*  
59  
60

1  
2  
3  
4 *al.*, 2010b; Shang *et al.*, 2011b; Buckley *et al.*, 2013; Zirak *et al.*, 2014), skeletal muscles  
5  
6  
7 (Henry *et al.*, 2015; Mesquita *et al.*, 2013; Yu *et al.*, 2005a; Shang *et al.*, 2012; Gurley *et al.*,  
8  
9 2012), and tumors (Chung *et al.*, 2015; Choe *et al.*, 2014; Zhou *et al.*, 2007; Durduran *et al.*,  
10  
11 2005; He *et al.*, 2015; Sunar *et al.*, 2006; Dong *et al.*, 2012b; Dong *et al.*, 2016). Since this  
12  
13 review focuses on the clinical applications, only typical clinical examples are presented in the  
14  
15 following subsections based on different types of tissues/organs. For more details, readers are  
16  
17 encouraged to read primary papers that are cited but not discussed here and to learn from  
18  
19 recent reviews (Yu, 2012a; Yu, 2012c; Durduran and Yodh, 2014; Mesquita *et al.*, 2011).  
20  
21  
22  
23  
24

### 25 **3.1 Brain**

#### 26 **3.1.1 Diagnosis of cardio-cerebral diseases**

27  
28  
29  
30  
31 DCS has been explored for the diagnosis and evaluation of cardio-cerebral diseases  
32  
33 affecting cerebral blood flow (CBF) in adults, children, and neonates. For example, DCS was  
34  
35 utilized to investigate CBF responses in adult patients with cerebral diseases including  
36  
37 vasovagal syncope (Cheng *et al.*, 2014), obstructive sleep apnea-hypopnea (Hou *et al.*, 2014;  
38  
39 Busch *et al.*, 2016a), traumatic brain injury (Kim *et al.*, 2010; Kim *et al.*, 2014), and ischemic  
40  
41 stroke (Durduran *et al.*, 2009; Favilla *et al.*, 2014).  
42  
43  
44  
45  
46  
47

48 Vasovagal syncope (VVS) is the sudden loss of consciousness, which can be fatal if  
49  
50 occurring in public such as driving and flying. In a study of CBF variations to predict VVS  
51  
52 (Cheng *et al.*, 2014), a 70-degree head-up-titling (HUT) protocol was applied to 14 healthy  
53  
54 adults, and relative changes of CBF (rCBF) to the baseline were continuously monitored  
55  
56 using a fiber-optic probe illustrated in **Fig. 3a**. In addition, relative changes of main artery  
57  
58 blood pressure (rMAP) were also continuously monitored using a noninvasive finger sensor  
59  
60



1  
2  
3  
4 (Portapres, FMS Inc., Netherlands). In the subjects having presyncope symptoms during HUT,  
5  
6  
7 physiological responses to the tilting were observed to have two stages; while Stage I showed  
8  
9  
10 a small changes, Stage II demonstrated a rapid and dramatic decreases in both rCBF and  
11  
12 rMAP that were coincided with presyncope symptoms (**Fig. 5**). On average, rCBF reached the  
13  
14 Stage II earlier and decreased larger ( $76 \pm 8\%$ , from a baseline of 100%) than rMAP ( $39 \pm$   
15  
16  $19\%$ , assigning a baseline value of 100%) during presyncope. Moreover, a threshold of  $\sim 50\%$   
17  
18 rCBF decline was determined to completely separate the subjects with or without presyncope.  
19  
20  
21  
22 This study suggests that continuous monitoring of CBF variations by the portable DCS device  
23  
24  
25 may provide predictive information to prevent VVS (e.g., using an automatic feedback to  
26  
27  
28 maintain MAP and CBF at normal levels).  
29  
30

31  
32 Another example of DCS applications is the study of obstructive sleep apnea-hypopnea  
33  
34 (OSAH) (Hou *et al.*, 2014), a disease characterized by repetitive pausing of breath resulted  
35  
36 from upper airway obstruction during sleep. The impeded airflow during OSAH may cause  
37  
38 cerebral ischemia and disturb CBF. Although OSAH can be diagnosed through monitoring of  
39  
40 overnight sleep with a polysomnography, evaluation of cerebral ischemia and hypoxia  
41  
42 induced by OSAH is not routinely conducted, due to lack of appropriately technologies.  
43  
44  
45 Using a dual-wavelength DCS flow-oximeter (Shang *et al.*, 2009), our group conducted  
46  
47  
48 continuous and simultaneous measurements of relative changes of CBF, oxy- and deoxy- and  
49  
50  
51 total hemoglobin concentrations (rCBF,  $\Delta[\text{HbO}_2]$ ,  $\Delta[\text{Hb}]$ ,  $\Delta\text{THC}$ ) in adult subjects with  
52  
53  
54 OSAH for  $\sim 8$  hours overnight (Hou *et al.*, 2014). Two fiber-optic probes connected to the  
55  
56  
57 DCS flow-oximeter were taped on both sides of the subject's forehead for cerebral monitoring  
58  
59  
60 during sleep (illustrated in **Fig. 3b**). To minimize the disturbance to patients, we remotely

1  
2  
3  
4 operated the optical measurements in a control room and designed special fiber-optic  
5  
6  
7 connectors which could easily disconnect the probes when the patient went to bathroom. The  
8  
9  
10 results showed that apneic events caused significant variations in rCBF and  $\Delta$ THC. Moreover,  
11  
12 the degrees of these hemodynamic variations were significantly correlated with the severity of  
13  
14  
15 OSAH.  
16

17  
18 Similarly, DCS was also adopted to measure CBF responses to hypercapnia during  
19  
20 wakefulness rather than during sleep in children with obstructive sleep syndrome (OSA)  
21  
22 and/or snores (Busch *et al.*, 2016a). Both OSA and snore subjects were found to have  
23  
24  
25 significant less changes in CBF during hypercapnia than health controls, indicating the  
26  
27  
28 diseased-induced blunted brain responses.  
29

30  
31 DCS was also utilized to monitor CBF variations in adults with traumatic brain injury  
32  
33 (Kim *et al.*, 2014; Kim *et al.*, 2010) or ischemic stroke (Favilla *et al.*, 2014; Durduran *et al.*,  
34  
35  
36 2009). In those studies, CBF changes were found to be associated with large variations in  
37  
38  
39 cerebral blood pressure induced by physiological manipulations (Kim *et al.*, 2010; Favilla *et*  
40  
41  
42 *al.*, 2014; Durduran *et al.*, 2009), indicating the impairments of cerebral autoregulation to  
43  
44  
45 maintain a constant CBF.  
46

47  
48 In addition to the applications in adults and children, DCS was employed to assess CBF  
49  
50  
51 in neonates with malfunctions/defects and during surgical treatments, including those with  
52  
53  
54 congenital heart disease (CHD) (Durduran *et al.*, 2010b) , hypoxic ischemic encephalopathy  
55  
56  
57 (Dehaes *et al.*, 2014), single-ventricle CHD undergoing surgery (Dehaes *et al.*, 2015), as well  
58  
59  
60 as the neonates during open heart surgery (Busch *et al.*, 2016b). In those studies, DCS

1  
2  
3  
4 measurements benefited from higher signal-to-noise ratio (SNR) due to the thinner skulls of  
5  
6  
7 neonates.

8  
9  
10 When subjected to a protocol of CO<sub>2</sub> inhalation for inducing hypercapnia (Durduran *et*  
11  
12 *al.*, 2010b), CBF values in neonates with CHD were elevated significantly ( $158 \pm 6\%$ ,  
13  
14 assigning a baseline of 100%), which were detectable by both DCS and ASL-MRI  
15  
16 measurements. Since complex CHD may lead to impaired cerebral autoregulation and  
17  
18 low-baseline CBF, this study explored the potential of DCS for longitudinally probing  
19  
20 cerebral defects in critically ill neonates.  
21  
22  
23

24  
25  
26 Apart from physiological challenging mentioned above, CBF values before and after  
27  
28 heart surgeries were measured and compared between the neonates with single-ventricle CHD  
29  
30 and healthy controls (Dehaes *et al.*, 2015). The results showed impaired cerebral development  
31  
32 in diseased neonates, as characterized by decreased CBF. Furthermore, CBF was  
33  
34 continuously monitored during neonatal open heart surgery, an intervention aiming to treat  
35  
36 heart defects (Busch *et al.*, 2016b). Significant variations in CBF during deep hypothermia,  
37  
38 circulatory arrest, and rewarming were observed, indicating the capability of DCS for cerebral  
39  
40 hemodynamic monitoring in a highly challenging clinical environment.  
41  
42  
43  
44  
45  
46

47  
48 In study of cerebral hemodynamics in premature neonates (Roche-Labarbe *et al.*, 2010),  
49  
50 a steady increase (28%, from a baseline of 100%) in CBF was found over the first six weeks  
51  
52 of life, indicating that the neonates gained improvements in brain microcirculation since birth.  
53  
54 In another study of extremely preterm neonates, the subjects with hemorrhage were found to  
55  
56 have lower CBF when compared with those without hemorrhage (Lin *et al.*, 2016). Similarly,  
57  
58  
59  
60

1  
2  
3  
4 lower CBF levels in neonates with hypoxic ischemic encephalopathy were reported,  
5  
6 compared to age-matched healthy neonates (Dehaes *et al.*, 2014).  
7  
8

9  
10 In summary, many cardio-cerebral diseases affect nervous system, cerebral  
11  
12 microvasculature, and cerebral oxygen kinetics, leading to abnormality in CBF (Durduran and  
13  
14 Yodh, 2014; Mesquita *et al.*, 2011). Therefore, CBF is considered as an important biomarker  
15  
16 of brain health, which links the oxygen demand, supply, and consumption. Continuous  
17  
18 measurements of CBF in the clinical setting, however, are not easily achievable due to  
19  
20 technology unavailability. DCS offers a continuous, fast, portable, and low-cost tool to  
21  
22 noninvasively monitor CBF variations at the bedside of the clinic. Studies presented in this  
23  
24 subsection demonstrate that CBF abnormalities are associated with a variety of cerebral  
25  
26 diseases. While the explicit relationships between CBF abnormalities and clinical outcomes  
27  
28 need to be further investigated, these studies support DCS as a useful tool for the diagnosis of  
29  
30 cerebral diseases in adults, children, and neonates.  
31  
32  
33  
34  
35  
36  
37  
38

### 39 **3.1.2 Therapeutic monitoring of cardio-cerebral diseases**

40  
41 DCS has been used to evaluate the effects of surgical interventions on CBF in adults and  
42  
43 infants. Those surgeries included carotid endarterectomy in adults (Shang *et al.*, 2011b),  
44  
45 thrombolysis in adults (Zirak *et al.*, 2014), and cardiac surgery in infants (Buckley *et al.*,  
46  
47 2013).  
48  
49  
50

51  
52 Carotid endarterectomy (CEA) is a surgical intervention to restore the blood supply to  
53  
54 brain through removal of the blockage in carotid artery (Shang *et al.*, 2011b). During CEA,  
55  
56 some of major vessels are temporarily clamped, causing a shutdown of blood supply to local  
57  
58 cerebral tissues. Thus, intraoperative monitoring of CBF variation is particularly important as  
59  
60

1  
2  
3  
4 it permits acute assessment of cerebral hemodynamic level during surgery and post-surgical  
5  
6 hemodynamic improvement in the brain. Electroencephalography (EEG) is an often-used  
7  
8 technology for cerebral monitoring during CEA, which offers indirect assessment of cerebral  
9  
10 ischemia through analysis of brain waves. In a comparison study of EEG and DCS  
11  
12 measurements for evaluating cerebral hemodynamic variations during CEA, EEG electrodes  
13  
14 were placed all over the scalps of eleven patients undergoing CEA, and two optical probes  
15  
16 were taped on both sides of forehead for simultaneous measurements of CBF and cerebral  
17  
18 oxygenation. The internal carotid artery (ICA) clamps during CEA resulted in significant  
19  
20 CBF decreases ( $-24.7 \pm 7.3\%$ , assigning a baseline of 100%) at the surgical sides (**Fig. 6a**).  
21  
22 On the other hand, post-CEA CBF values were significantly higher ( $+43.2 \pm 16.9\%$ , assigning  
23  
24 a baseline of 100%) than pre-CEA CBF values. Flow compensation via circle of Willis was  
25  
26 also observed at the nonsurgical side (**Fig. 6b**). CBF responses to ICA clamping were found  
27  
28 to be significantly faster, larger, and more sensitive than EEG responses (**Fig.7**).  
29  
30 Simultaneous monitoring of CBF and EEG provided a comprehensive evaluation of cerebral  
31  
32 physiological status and showed potential for the adoption of acute interventions (e.g.,  
33  
34 shunting, medications) during CEA to reduce the risks of severe cerebral ischemia and  
35  
36 cerebral hyperperfusion syndrome.  
37  
38  
39  
40  
41  
42  
43  
44  
45  
46  
47  
48

49 DCS was also applied to a patient with acute ischemic stroke, who received  
50  
51 thrombolytic therapy to restore CBF (Zirak *et al.*, 2014). CBF was monitored by DCS  
52  
53 throughout the 60-minute thrombolytic therapy. DCS data showed an acute improvement in  
54  
55 CBF after thrombolytic therapy, which agreed with the improvement in stroke scale score.  
56  
57  
58  
59  
60 This study suggested the potential of continuous DCS monitoring for therapeutic evaluation

1  
2  
3  
4 of acute stroke.  
5

6  
7 DCS measurements of CBF during interventions were also reported in infants. For  
8  
9 example, CBF, cerebral oxygenation, and cerebral oxygen metabolism were continuously  
10  
11 monitored during the period of postoperative neonatal cardiac surgery using a hybrid optical  
12  
13 instrument (Buckley *et al.*, 2013). Due to the complicated communications between the  
14  
15 cerebral and cardiac vessels, the surgeries on hearts were found to significantly affect cerebral  
16  
17 oxygen extraction fraction, but not CBF and cerebral metabolic rate of oxygen consumption.  
18  
19  
20  
21

22  
23 In summary, many intervention strategies for cardio-cerebral diseases are to restore  
24  
25 tissue blood flow. Studies presented in this subsection show high sensitivity of DCS for  
26  
27 continuous monitoring of CBF variations during interventions, which holds the potential for  
28  
29 dynamic assessment and optimization of cardio-cerebral interventions to maintain CBF in a  
30  
31 normal level.  
32  
33  
34

## 35 36 37 **3.2 Skeletal muscle**

### 38 39 40 **3.2.1 Diagnosis of muscular diseases**

41  
42  
43 DCS has been adopted to evaluate the vascular diseases affecting skeletal muscle  
44  
45 perfusion such as fibromyalgia and peripheral arterial disease (Shang *et al.*, 2012; Mesquita *et*  
46  
47 *al.*, 2013). Evaluation of muscular diseases was often performed in a dynamic manner  
48  
49 because those diseases restrict patients from performing leg or arm exercises. Blood flow  
50  
51 responses to exercise reflect how skeletal muscles properly perform physiological functions.  
52  
53  
54

55  
56  
57 In a study of fibromyalgia (FM) (Shang *et al.*, 2012), women with FM were instructed to  
58  
59 perform knee extension exercises with steadily increasing intensity. Calf muscle  
60

1  
2  
3  
4 hemodynamics was continuously monitored by a hybrid instrument during exercise using a  
5  
6 probe illustrated in **Fig. 3c**. Results showed that subjects with FM had significantly lower  
7  
8 oxygen extraction rate during exercise than healthy controls, and the time of oxygenation  
9  
10 recovery were significantly longer. These results suggested an alteration of muscle oxygen  
11  
12 utilization in the FM population.  
13  
14  
15  
16

17  
18 In another study investigating the influence of peripheral arterial disease (PAD) on  
19  
20 skeletal muscle hemodynamics (Mesquita *et al.*, 2013), calf blood flow values were found to  
21  
22 occur at more depressed levels in PAD population after treadmill and pedal exercises,  
23  
24 compared to those in age-matched healthy people. These results indicated adverse impact of  
25  
26 PAD on blood flow responses to exercise.  
27  
28  
29  
30

31  
32 Limitations existed when using DCS techniques to continuously monitor muscle  
33  
34 hemodynamic changes *during* exercise, such as the nature of relative measurement (rBF) and  
35  
36 the motion artifact induced by the exercise. To overcome these limitations, our group recently  
37  
38 created a calibration protocol for absolute flow measurements and a gating algorithm to  
39  
40 minimize motion artifacts during exercise (Gurley *et al.*, 2012; Henry *et al.*, 2015). Briefly, a  
41  
42 hybrid DCS/NIRS instrument along with a pre-exercise arterial occlusion protocol was  
43  
44 utilized to quantify the absolute baseline blood flow value before exercise. The absolute  
45  
46 baseline flow value was then used to calibrate the measured rBF during exercise in order to  
47  
48 obtain absolute flow measurements over the entire exercising period. Motion artifacts were  
49  
50 minimized using a novel dynamometer-based gating algorithm embedded in the DCS control  
51  
52 software. Essentially, this software determined muscle contraction status based on signals  
53  
54 from the dynamometer and recorded data only when muscle fiber motion was minimal.  
55  
56  
57  
58  
59  
60

1  
2  
3  
4 The innovative calibration and gating algorithms have been recently applied on patients  
5  
6 with FM and compared with age-matched healthy controls. Blood flow responses in forearm  
7  
8 muscles to handgrip exercise were continuously monitored and patients with FM exhibited  
9  
10 less capability to perform handgrip exercise than healthy controls, evidenced by the weaker  
11  
12 blood flow responses during exercise (**Fig. 8**).  
13  
14  
15  
16

17 Overall, deficiency of skeletal muscle function may result from mitochondrial  
18  
19 dysfunction (Cordero *et al.*, 2010), lower capillary density (Lindh *et al.*, 1995; Morf *et al.*,  
20  
21 2005), reduced capillary permeability (Grassi *et al.*, 1994) and impaired vasodilatory capacity  
22  
23 (Kasikcioglu *et al.*, 2006; McIver *et al.*, 2006), all of which are difficult to measure  
24  
25 noninvasively. Hybrid DCS/NIRS devices enable noninvasive dynamic quantification of  
26  
27 blood flow, blood oxygenation, and oxidative metabolism during exercise, providing unique  
28  
29 and comprehensive diagnostic information for skeletal muscle diseases.  
30  
31  
32  
33  
34  
35

### 36 **3.2.2 Therapeutic monitoring of muscular diseases**

37

38 A few studies have been reported using DCS to investigate the impacts of surgical  
39  
40 interventions on skeletal muscle diseases (Yu *et al.*, 2011; Huang *et al.*, 2015c). For muscular  
41  
42 revascularization, ultrasound Doppler is routinely used in surgical rooms to test post-surgical  
43  
44 reperfusion in large vessels. However, ultrasound Doppler cannot directly assess the  
45  
46 restoration of tissue microcirculation, which is generally the major goal of revascularization.  
47  
48  
49  
50  
51

52 Using a portable DCS flow-oximeter and the probe illustrated in **Fig. 3c** (Shang *et al.*,  
53  
54 2009), we continuously monitored calf muscle blood flow variations on twelve human limbs  
55  
56 undergoing artery revascularization (Yu *et al.*, 2011). The high sensitivity of DCS in  
57  
58 detecting blood flow changes was confirmed through clamping or ballooning on/off the  
59  
60



1  
2  
3  
4 femoral or aorta arteries during surgeries. Furthermore, immediate hyperemia following the  
5  
6  
7 release of occlusions and post-surgery flow improvements in calf muscles were observed,  
8  
9  
10 indicating the potential of the DCS for objective assessment of revascularization effects.

11  
12 Another representative application of DCS is the assessment of blood flow in free  
13  
14 transfer muscle flaps following salvage surgeries in patients with head and neck cancer.  
15  
16  
17 Conventional approaches to evaluate the success of tissue flaps rely on visual examination  
18  
19 along with blood flow measurements in large vessels by ultrasound Doppler. DCS offers a  
20  
21  
22 tool to directly assess tissue blood flow in peripheral muscle flaps, which is crucial to  
23  
24  
25 evaluate the success of surgeries. For intraoperative monitoring of reconstructive flaps, we  
26  
27  
28 designed a lens system which focused the sources and detectors on the tissue surface,  
29  
30  
31 permitting noncontact measurements of flap blood flow (see **Fig. 3f**) (Huang *et al.*, 2015c).  
32  
33  
34 The noncontact DCS probe was applied to eight free muscle flaps at multiple time points of  
35  
36  
37 blood flow measurements during and post the surgical operations. **Fig. 9** shows comparison  
38  
39  
40 results obtained from seven successful flaps and one unsuccessful flap. Postoperative blood  
41  
42  
43 flow values in the successful flaps were significantly higher than the intraoperative baseline  
44  
45  
46 values, indicating a gradual recovery of flap vascularity after the tissue transfer. By contrast,  
47  
48  
49 postoperative blood flow recovered much less in the unsuccessful flap. Measurement of blood  
50  
51  
52 flow recovery after flap anastomosis holds the potential to act early to salvage ischemic flaps.

### 52 **3.3 Tumor**

#### 53 54 55 **3.3.1 Diagnosis of tumors**

56  
57  
58 The first translational case of DCS for clinical cancer diagnosis was reported on human  
59  
60 breast tumors (Durduran *et al.*, 2005). Through scanning over the breast tumors (n = 5) using

1  
2  
3  
4 a contact optical probe illustrated in **Fig. 3d**, higher blood flow contrasts were found in  
5  
6 malignant (230% by averaging over three subjects) and benign (153% by averaging over two  
7  
8 subjects) tumors, respectively, as compared to the surrounding normal tissues (assigning  
9  
10 100%). Similar measurement configuration was thereafter applied to a larger population with  
11  
12 breast tumors (n = 32) (Choe *et al.*, 2014), confirming the high blood flow contrasts in breast  
13  
14 tumors (225~227% in mean value and 190~270% in 95% confidence intervals).  
15  
16  
17  
18  
19

20  
21 Moreover, a recent pilot study investigated the correlations between tumor hemodynamic  
22  
23 parameters (i.e., blood flow, [HbO<sub>2</sub>], [Hb], StO<sub>2</sub>, THC) and tumor histopathological  
24  
25 biomarkers. Increased blood supply to breast tumors was observed, which agreed with the  
26  
27 high expression level of Ki67 nuclei in the confirmed breast tumors (Chung *et al.*, 2015). This  
28  
29 study suggested that the macroscopic measurements of tissue hemodynamics could reveal  
30  
31 pathological properties of breast cancer in microscopic level.  
32  
33  
34  
35

36  
37 A significant problem with contact DCS measurements described above is the deformation  
38  
39 of soft breast tissue, which may distort blood flow distribution in the soft breast. To solve this  
40  
41 problem, noncontact DCS/DCT (ncDCS/ncDCT) systems with unique fiber-optic probes were  
42  
43 recently developed enabling fully noncontact measurement/imaging of blood distributions in  
44  
45 deep tissue volumes with complex boundaries (Lin *et al.*, 2014; Lin *et al.*, 2012; Li *et al.*,  
46  
47 2013; Huang *et al.*, 2015c; He *et al.*, 2015; Huang *et al.*, 2015b). The noncontact probe was  
48  
49 attached to a motorized stage that scanned linearly or rotationally over a ROI (**Fig. 4**). **Fig. 10**  
50  
51 shows *in vivo* imaging results from two breast carcinomas. Higher blood flow contrasts (5.9-  
52  
53 and 10.9-fold) in the tumor regions compared to the surrounding tissues were observed. The  
54  
55 reconstructed locations of the two tumors matched ultrasound imaging results when the tumor  
56  
57  
58  
59  
60

1  
2  
3  
4 was within the sensitivity region of diffuse light. The ncDCT system showed the promise to  
5  
6  
7 image blood flow distributions in soft and vulnerable tissues without distorting tissue  
8  
9  
10 hemodynamics.

11  
12 The autonomic growth and spread of tumors are dependent on increased angiogenesis  
13  
14 arising from the increased metabolic demand. Since functional alternations in tumors often  
15  
16  
17 appear earlier than detectable morphological changes, functional imaging of tumor blood flow  
18  
19  
20 by DCT is a new strategy for early cancer diagnosis and localization.  
21

### 22 **3.3.2 Therapeutic monitoring of tumor treatments**

23  
24  
25 It has been found that the patients with hypoxic tumors show incomplete clinical  
26  
27  
28 responses when receiving chemo-radiation therapy that requires tissue oxygen for treatment  
29  
30  
31 efficacy (Busch *et al.*, 2000; Carlson, 2006). Many tumors are hypoxic because of abnormal  
32  
33  
34 vasculature, malignancy-related anemia, and/or high oxygen consumption by tumor cells.  
35  
36  
37 Studies have shown that pretreatment tumor hypoxia is associated with significantly poor  
38  
39  
40 responses to the therapy when compared to oxygenated tumors. However, some  
41  
42  
43 well-oxygenated tumors failed to respond while some hypoxic tumors responded well,  
44  
45  
46 possibly due to the dynamic changes during treatment in tumor oxygen status induced by  
47  
48  
49 radiation. Therefore, repeated monitoring of individual tumor hemodynamic status during  
50  
51  
52 therapy may provide predictive information for treatment outcomes.

53  
54 To date, DCS has been utilized to monitor the tumor hemodynamic responses to  
55  
56  
57 chemo-radiation therapy in breast tumors (Zhou *et al.*, 2007) and head/neck tumors (Sunar *et*  
58  
59  
60 *al.*, 2006; Dong *et al.*, 2012b; Dong *et al.*, 2016). In a case study of breast cancer using a  
hybrid DCS/NIRS device, significant changes in tumor blood flow and blood oxygenation

1  
2  
3  
4 were observed in the first week of chemo-radiation therapy (Zhou *et al.*, 2007).  
5  
6

7 In another pilot study of head/neck tumors using a hybrid DCS/NIRS instrument, tumor  
8  
9 hemodynamic responses in a small group of patients (n = 8) were continually measured once  
10  
11 a week over the period of chemo-radiation therapy (Sunar *et al.*, 2006). Tumors exhibited  
12  
13 significant dynamic flow and oxygenation changes during the first four weeks of the  
14  
15 treatment. This study, however, was limited by the small number of patients examined and  
16  
17 only one patient out of 8 showed a partial response to the treatment.  
18  
19  
20  
21

22  
23 Very recently, our group employed a hybrid DCS/NIRS instrument to continually  
24  
25 monitor tumor hemodynamic responses to chemo-radiation therapy for early prediction of  
26  
27 treatment outcomes in a relative large patient population with head/neck cancers (Dong *et al.*,  
28  
29 2016). Forty-seven patients were measured once per week over 7 weeks of treatment period to  
30  
31 evaluate the hemodynamic status of clinically involved cervical lymph nodes. Patients were  
32  
33 classified into two groups: complete response (CR) (n = 29) and incomplete response (IR) (n  
34  
35 = 18). Interestingly, tumor hemodynamic responses were found to be associated with clinical  
36  
37 outcomes (CR/IR), wherein the associations differed depending on human papillomavirus  
38  
39 (HPV-16) status. In HPV-16 positive patients, significantly lower levels in tumor [HbO<sub>2</sub>] at  
40  
41 weeks 1 to 3, THC at week 3, and StO<sub>2</sub> at week 3 were found in the IR group. In HPV-16  
42  
43 negative patients, significantly higher levels in tumor BFI and  $\mu_s'$  at week 3 were observed in  
44  
45 the IR group. These hemodynamic parameters exhibited significantly high accuracies for  
46  
47 early prediction of clinical outcomes, within the first three weeks of therapy, with the areas  
48  
49 under the receiver operating characteristic curves (AUCs) ranging from 0.83 to 0.96 (**Fig. 11**).  
50  
51  
52  
53  
54  
55  
56  
57  
58  
59  
60

1  
2  
3  
4 Overall, tumor hemodynamic parameters exhibited significantly high accuracies for early  
5  
6 prediction of clinical outcomes. Such predications, based on frequent optical measurements,  
7  
8 may ultimately be used to optimize individual therapeutic outcomes at an early time of  
9  
10 therapy. For example, treatment outcomes may be improved by dynamically promoting  
11  
12 oxygenation levels (e.g., hyperbaric oxygen therapy) in HPV-16 positive tumors or inhibiting  
13  
14 angiogenesis (e.g., anti-VEGF antibody) in HPV-16 negative tumors.  
15  
16  
17  
18  
19

#### 20 **4. Summary and future perspectives**

21  
22  
23 In contrast to large imaging modalities such as CT, MRI, and PET, optical instruments  
24  
25 such as NIRS/DOS/DOT and DCS/DCT are portable, fast, inexpensive, and suitable for  
26  
27 continuous measurements at the bedside of clinical settings. NIRS/DOS/DOT techniques have  
28  
29 been extensively used to measure tissue oxygenation in the clinic. Compared to  
30  
31 NIRS/DOS/DOT, DCS/DCT is a relatively new technique that enables direct measurement of  
32  
33 tissue blood flow. DCS/DCT or hybrid DCS/NIRS is being increasingly employed worldwide  
34  
35 in a large variety of clinical contexts for the diagnosis and therapeutic monitoring of various  
36  
37 diseases affecting tissue hemodynamics and metabolism. Overall, these pilot clinical studies  
38  
39 in relatively small populations have shown the technique's versatility and demonstrated that  
40  
41 the method provides new and complementary information about patient pathophysiology in a  
42  
43 noninvasive fashion. It should be noticed that DCS/DCT has only been applied to a small  
44  
45 population of patients with short measurement time frames (minutes to several weeks).  
46  
47  
48  
49  
50  
51  
52  
53  
54  
55  
56  
57  
58  
59  
60  
61  
62  
63  
64  
65  
66  
67  
68  
69  
70  
71  
72  
73  
74  
75  
76  
77  
78  
79  
80  
81  
82  
83  
84  
85  
86  
87  
88  
89  
90  
91  
92  
93  
94  
95  
96  
97  
98  
99  
100  
101  
102  
103  
104  
105  
106  
107  
108  
109  
110  
111  
112  
113  
114  
115  
116  
117  
118  
119  
120  
121  
122  
123  
124  
125  
126  
127  
128  
129  
130  
131  
132  
133  
134  
135  
136  
137  
138  
139  
140  
141  
142  
143  
144  
145  
146  
147  
148  
149  
150  
151  
152  
153  
154  
155  
156  
157  
158  
159  
160  
161  
162  
163  
164  
165  
166  
167  
168  
169  
170  
171  
172  
173  
174  
175  
176  
177  
178  
179  
180  
181  
182  
183  
184  
185  
186  
187  
188  
189  
190  
191  
192  
193  
194  
195  
196  
197  
198  
199  
200  
201  
202  
203  
204  
205  
206  
207  
208  
209  
210  
211  
212  
213  
214  
215  
216  
217  
218  
219  
220  
221  
222  
223  
224  
225  
226  
227  
228  
229  
230  
231  
232  
233  
234  
235  
236  
237  
238  
239  
240  
241  
242  
243  
244  
245  
246  
247  
248  
249  
250  
251  
252  
253  
254  
255  
256  
257  
258  
259  
260  
261  
262  
263  
264  
265  
266  
267  
268  
269  
270  
271  
272  
273  
274  
275  
276  
277  
278  
279  
280  
281  
282  
283  
284  
285  
286  
287  
288  
289  
290  
291  
292  
293  
294  
295  
296  
297  
298  
299  
300  
301  
302  
303  
304  
305  
306  
307  
308  
309  
310  
311  
312  
313  
314  
315  
316  
317  
318  
319  
320  
321  
322  
323  
324  
325  
326  
327  
328  
329  
330  
331  
332  
333  
334  
335  
336  
337  
338  
339  
340  
341  
342  
343  
344  
345  
346  
347  
348  
349  
350  
351  
352  
353  
354  
355  
356  
357  
358  
359  
360  
361  
362  
363  
364  
365  
366  
367  
368  
369  
370  
371  
372  
373  
374  
375  
376  
377  
378  
379  
380  
381  
382  
383  
384  
385  
386  
387  
388  
389  
390  
391  
392  
393  
394  
395  
396  
397  
398  
399  
400  
401  
402  
403  
404  
405  
406  
407  
408  
409  
410  
411  
412  
413  
414  
415  
416  
417  
418  
419  
420  
421  
422  
423  
424  
425  
426  
427  
428  
429  
430  
431  
432  
433  
434  
435  
436  
437  
438  
439  
440  
441  
442  
443  
444  
445  
446  
447  
448  
449  
450  
451  
452  
453  
454  
455  
456  
457  
458  
459  
460  
461  
462  
463  
464  
465  
466  
467  
468  
469  
470  
471  
472  
473  
474  
475  
476  
477  
478  
479  
480  
481  
482  
483  
484  
485  
486  
487  
488  
489  
490  
491  
492  
493  
494  
495  
496  
497  
498  
499  
500  
501  
502  
503  
504  
505  
506  
507  
508  
509  
510  
511  
512  
513  
514  
515  
516  
517  
518  
519  
520  
521  
522  
523  
524  
525  
526  
527  
528  
529  
530  
531  
532  
533  
534  
535  
536  
537  
538  
539  
540  
541  
542  
543  
544  
545  
546  
547  
548  
549  
550  
551  
552  
553  
554  
555  
556  
557  
558  
559  
560  
561  
562  
563  
564  
565  
566  
567  
568  
569  
570  
571  
572  
573  
574  
575  
576  
577  
578  
579  
580  
581  
582  
583  
584  
585  
586  
587  
588  
589  
590  
591  
592  
593  
594  
595  
596  
597  
598  
599  
600  
601  
602  
603  
604  
605  
606  
607  
608  
609  
610  
611  
612  
613  
614  
615  
616  
617  
618  
619  
620  
621  
622  
623  
624  
625  
626  
627  
628  
629  
630  
631  
632  
633  
634  
635  
636  
637  
638  
639  
640  
641  
642  
643  
644  
645  
646  
647  
648  
649  
650  
651  
652  
653  
654  
655  
656  
657  
658  
659  
660  
661  
662  
663  
664  
665  
666  
667  
668  
669  
670  
671  
672  
673  
674  
675  
676  
677  
678  
679  
680  
681  
682  
683  
684  
685  
686  
687  
688  
689  
690  
691  
692  
693  
694  
695  
696  
697  
698  
699  
700  
701  
702  
703  
704  
705  
706  
707  
708  
709  
710  
711  
712  
713  
714  
715  
716  
717  
718  
719  
720  
721  
722  
723  
724  
725  
726  
727  
728  
729  
730  
731  
732  
733  
734  
735  
736  
737  
738  
739  
740  
741  
742  
743  
744  
745  
746  
747  
748  
749  
750  
751  
752  
753  
754  
755  
756  
757  
758  
759  
760  
761  
762  
763  
764  
765  
766  
767  
768  
769  
770  
771  
772  
773  
774  
775  
776  
777  
778  
779  
780  
781  
782  
783  
784  
785  
786  
787  
788  
789  
790  
791  
792  
793  
794  
795  
796  
797  
798  
799  
800  
801  
802  
803  
804  
805  
806  
807  
808  
809  
810  
811  
812  
813  
814  
815  
816  
817  
818  
819  
820  
821  
822  
823  
824  
825  
826  
827  
828  
829  
830  
831  
832  
833  
834  
835  
836  
837  
838  
839  
840  
841  
842  
843  
844  
845  
846  
847  
848  
849  
850  
851  
852  
853  
854  
855  
856  
857  
858  
859  
860  
861  
862  
863  
864  
865  
866  
867  
868  
869  
870  
871  
872  
873  
874  
875  
876  
877  
878  
879  
880  
881  
882  
883  
884  
885  
886  
887  
888  
889  
890  
891  
892  
893  
894  
895  
896  
897  
898  
899  
900  
901  
902  
903  
904  
905  
906  
907  
908  
909  
910  
911  
912  
913  
914  
915  
916  
917  
918  
919  
920  
921  
922  
923  
924  
925  
926  
927  
928  
929  
930  
931  
932  
933  
934  
935  
936  
937  
938  
939  
940  
941  
942  
943  
944  
945  
946  
947  
948  
949  
950  
951  
952  
953  
954  
955  
956  
957  
958  
959  
960  
961  
962  
963  
964  
965  
966  
967  
968  
969  
970  
971  
972  
973  
974  
975  
976  
977  
978  
979  
980  
981  
982  
983  
984  
985  
986  
987  
988  
989  
990  
991  
992  
993  
994  
995  
996  
997  
998  
999  
1000

1  
2  
3  
4       There has been a concern on the physical modeling of blood flow (i.e., the motion of red  
5  
6  
7 blood cells) in the microvasculature. It was found that diffusive motion (see Section 2.1) fits  
8  
9  
10 the experimental autocorrelation curves rather well over a broad range of tissue types  
11  
12 (Durduran, 2004; Zhou, 2007). Intuitively, however, random ballistic flow would be  
13  
14 considered as a better model to fit the DCS/DCT data. Modified mixture models were  
15  
16 proposed to include both ballistic flow and diffusive motion (Carp *et al.*, 2011; Boas *et al.*,  
17  
18 2016). Experimental data supported the proposed models for capturing the transition from  
19  
20 early ballistic to subsequent diffusive motion. Computer simulations on the tissue with varied  
21  
22 vessel diameters and spacing showed that the diffusive motion dominates the correlation  
23  
24 decay in typical DCS measurements, and the blood flow index is modulated proportionally by  
25  
26 the concentration of hemoglobin and the average diameter of blood vessels. Nevertheless,  
27  
28 more clinical investigations are needed for accurate extracting of blood flow information in  
29  
30 deep tissues.  
31  
32  
33  
34  
35  
36  
37

38  
39       Some technical issues exist when applying NIR diffuse optical technologies to deep  
40  
41 tissues with heterogeneous properties. Since NIRS and DCS techniques rely on the transport  
42  
43 of NIR light through top layer tissues (e.g., skin, skull), both methods must account for partial  
44  
45 volume contributions from the top layer-structure to the deep tissue signals (e.g., brain,  
46  
47 muscle, and tumor). In addition, measurement signal-to-noise ratio (SNR) and penetration  
48  
49 depth are two interrelated and important parameters that affect the utility of both DCS and  
50  
51 NIRS. Furthermore, most research with DCS reports only relative changes of blood flow  
52  
53 index with respect to some baseline condition.  
54  
55  
56  
57  
58  
59  
60

1  
2  
3  
4 The “partial volume effect” substantially affects the accuracy of DCS measurements, as  
5  
6  
7 discussed in literature (Durduran and Yodh, 2014; Yu, 2012a; Strangman *et al.*, 2003).  
8  
9 Slab-layered models were proposed to reduce the partial volume effect (Jaillon *et al.*, 2006; Li  
10  
11 *et al.*, 2005; Verdecchia *et al.*, 2016). A recently developed method, “Modified Beer-Lambert  
12  
13 law for blood flow”, has been proved to be effective in pressure modulation experiments to  
14  
15 reduce the skin-effect on cerebral blood flow measurements (Baker *et al.*, 2014; Baker *et al.*,  
16  
17 2015). However, those methods ignored the influence of irregular tissue geometries. Recently,  
18  
19 we created a new algorithm integrating a linear model of autocorrelation function with the  
20  
21 Monte Carlo simulation of photon migrations in heterogeneous tissues with arbitrary  
22  
23 geometries for simultaneous extraction of blood flow indices in multiple layered tissues  
24  
25 (Shang and Yu, 2014).  
26  
27  
28  
29  
30  
31  
32

33 Compared to NIRS/DOS/DOT, DCS/DCT measurements have relatively lower SNRs  
34  
35 when probing deep tissue blood flow with large S-D separations (e.g., >2.5 mm). This is due  
36  
37 to the utilization of single-mode detector fibers with a small core diameter of 5  $\mu\text{m}$  in  
38  
39 DCS/DCT measurements to ensure the detection of autocorrelation functions of light intensity.  
40  
41 Efforts have been made to improve SNR through the spatial average of multiple  
42  
43 autocorrelation functions detected by a detector fiber bundle (Dietsche *et al.*, 2007) or the  
44  
45 temporal average of DCS signals obtained by a fast software correlator (Wang *et al.*, 2016).  
46  
47  
48  
49  
50  
51

52 A potential remedy for the absolute blood flow measurement problem is to calibrate  
53  
54 DCS/DCT against a gold standard. As mentioned early, comparison studies in small  
55  
56 populations have been done in skeletal muscles, tumors, and brains against other established  
57  
58 methods including power spectral Doppler ultrasound (Yu *et al.*, 2005b), Doppler ultrasound  
59  
60

1  
2  
3  
4 (Buckley *et al.*, 2009; Roche-Labarbe *et al.*, 2010), laser Doppler (Durduran, 2004; Shang *et*  
5  
6  
7 *al.*, 2011a), Xenon-CT (Kim *et al.*, 2010), fluorescent microsphere flow measurement (Zhou  
8  
9  
10 *et al.*, 2009), and ASL-MRI (Yu *et al.*, 2007). Results from these studies show the promise to  
11  
12 obtain absolute flow measurements although further validation works need to be done with  
13  
14  
15 different types of tissues in large populations.  
16

17  
18 DCT/ncDCT enables 3-D imaging of blood flow distributions in deep tissues. While  
19  
20 effective, ncDCS/ncDCT employs a limited number of expensive APDs for blood flow  
21  
22  
23 detection, leading to low spatiotemporal resolution and high instrument cost (Lin *et al.*, 2014;  
24  
25  
26 He *et al.*, 2015; Huang *et al.*, 2015b). With current ncDCT, the ROI must be mechanically  
27  
28 scanned for a complete tissue coverage, which can take up to 40 minutes and may result in  
29  
30  
31 motion artifacts. To overcome these limitations, we recently developed and tested a  
32  
33  
34 non-scanning, noncontact, fast, portable, cost-effective device, namely speckle contrast  
35  
36  
37 diffuse correlation tomography (scDCT), for 3-D imaging flow distributions (Huang *et al.*,  
38  
39  
40 2015a; Huang *et al.*, 2016). The scDCT used a charge-coupled-device (CCD) as a 2-D  
41  
42  
43 detector array to cover a ROI, thus eliminating the mechanical scanning and consequent  
44  
45  
46 problems. Thousands of detectors provided by the CCD significantly improved  
47  
48  
49 spatiotemporal resolution and reduced instrument cost/size. The scDCT prototype has been  
50  
51  
52 tested using computer simulations and tissue phantoms with anomaly flow contrast design.  
53  
54  
55 We are currently translating this novel optical technique to the clinic.

56  
57  
58 It is well known that many diseases are associated with tissue hypoxia, which is  
59  
60  
61 influenced by oxygen supply (i.e., blood flow) and tissue oxygen consumption. Simultaneous  
62  
63  
64 measurements of tissue blood flow and blood oxygenation using combined DCS and NIRS



1  
2  
3  
4 instruments enable the evaluation of tissue metabolic rate of oxygen consumption (Durduran  
5  
6 *et al.*, 2004; Roche-Labarbe *et al.*, 2010; Lin *et al.*, 2016; Dehaes *et al.*, 2014; Durduran *et al.*,  
7  
8 2010b; Buckley *et al.*, 2013; Henry *et al.*, 2015; Shang *et al.*, 2012; Gurley *et al.*, 2012;  
9  
10 Chung *et al.*, 2015). This metabolic parameter is potentially a more direct indicator of tissue  
11  
12 metabolic activities, which integrates many factors and provides further insight about tissue  
13  
14 pathophysiology. It is expected that with further technology development and more clinical  
15  
16 applications, DCS/DCT and hybrid DCS/NIRS technologies will be eventually utilized as  
17  
18 routine diagnostic and intervention monitoring tools for clinical investigations of various  
19  
20 diseases.  
21  
22  
23  
24  
25  
26  
27

### 28 **Acknowledgement**

29  
30  
31  
32 We acknowledge support from the National Institutes of Health (NIH) R01-CA149274,  
33  
34 R21-AR062356, and UL-1RR033173 Pilot Grant. We also acknowledge support of Research  
35  
36 Funds from the American Heart Association Grant-In-Aid #16GRNT30820006, National  
37  
38 Endowment for Plastic Surgery Grant 3048112770, National Science Foundation (NSF)  
39  
40 1539068, and the National Key Research and Development Program of China  
41  
42 2016YFC0101600. The content herein is solely the responsibility of the authors and does not  
43  
44 necessarily represent the official views of NIH and other foundations.  
45  
46  
47  
48  
49  
50  
51  
52  
53  
54  
55  
56  
57  
58  
59  
60

**References:**

- Al-Rawi P G and Kirkpatrick P J 2006 Tissue oxygen index - Thresholds for cerebral ischemia using near-infrared spectroscopy *Stroke* **37** 2720-5
- Arridge S R and Hebden J C 1997 Optical imaging in medicine: II. Modelling and reconstruction *Phys Med Biol* **42** 841-53
- Arridge S R and Lionheart W R 1998 Nonuniqueness in diffusion-based optical tomography *Opt Lett* **23** 882-4
- Baker W B, Parthasarathy A B, Busch D R, Mesquita R C, Greenberg J H and Yodh A G 2014 Modified Beer-Lambert law for blood flow *Biomed. Opt. Express* **5** 4053-75
- Baker W B, Parthasarathy A B, Ko T S, Busch D R, Abramson K, Tzeng S Y, Mesquita R C, Durduran T, Greenberg J H, Kung D K and Yodh A G 2015 Pressure modulation algorithm to separate cerebral hemodynamic signals from extracerebral artifacts *Neurophotonics* **2** 035004
- Boas D A 1996 Diffuse Photon Probes of Structural and Dynamical Properties of Turbid Media: Theory and Biomedical Applications University of Pennsylvania: Philadelphia, USA pp 1-244
- Boas D A, Campbell L E and Yodh A G 1995 Scattering and imaging with diffusing temporal field correlations *Phys. Rev. Lett.* **75** 1855-8
- Boas D A, Gaudette T, Strangman G, Cheng X F, Marota J J A and Mandeville J B 2001 The accuracy of near infrared spectroscopy and imaging during focal changes in cerebral hemodynamics *Neuroimage* **13** 76-90
- Boas D A, Sakadzic S, Selb J, Farzam P, Franceschini M A and Carp S A 2016 Establishing the diffuse correlation spectroscopy signal relationship with blood flow *Neurophotonics* **3** 031412
- Boas D A and Yodh A G 1997 Spatially varying dynamical properties of turbid media probed with diffusing temporal light correlation *Journal of the Optical Society of America a-Optics Image Science and Vision* **14** 192-215
- Bouye P, Jacquinand V, Picquet J, Thouveny F, Liagre J, Leftheriotis G, Saumet J L and Abraham P 2005 Near-infrared spectroscopy and transcutaneous oxygen pressure during exercise to detect arterial ischemia at the buttock level: Comparison with arteriography *J. Vasc. Surg.* **41** 994-9
- Brown W 1993 *Dynamic Light Scattering: The Method and Some Applications* Clarendon: New York
- Buckley E M, Cook N M, Durduran T, Kim M N, Zhou C, Choe R, Yu G, Shultz S, Sehgal C M, Licht D J, Arger P H, Putt M E, Hurt H and Yodh A G 2009 Cerebral hemodynamics in preterm infants during positional intervention measured with diffuse correlation spectroscopy and transcranial Doppler ultrasound *Opt. Express* **17** 12571-81
- Buckley E M, Lynch J M, Goff D A, Schwab P J, Baker W B, Durduran T, Busch D R, Nicolson S C, Montenegro L M, Naim M Y, Xiao R, Spray T L, Yodh A G, Gaynor J W and Licht D J 2013 Early postoperative changes in cerebral oxygen metabolism following neonatal cardiac surgery: Effects of surgical duration *Journal of Thoracic and Cardiovascular Surgery* **145** 196-205

- 1  
2  
3  
4 Busch D R, Lynch J M, Winters M E, McCarthy A L, Newland J J, Ko T, Cornaglia M A,  
5 Radcliffe J, McDonough J M, Samuel J, Matthews E, Xiao R, Yodh A G, Marcus C L,  
6 Licht D J and Tapia I E 2016a Cerebral Blood Flow Response to Hypercapnia in  
7 Children with Obstructive Sleep Apnea Syndrome *Sleep* **39** 209-16  
8  
9 Busch D R, Rusin C G, Miller-Hance W, Kibler K, Baker W B, Heinle J S, Fraser C D, Yodh  
10 A G, Licht D J and Brady K M 2016b Continuous cerebral hemodynamic  
11 measurement during deep hypothermic circulatory arrest *Biomed. Opt. Express* **7**  
12 3461-70  
13  
14 Busch T M, Hahn S M, Evans S M and Koch C J 2000 Depletion of tumor oxygenation  
15 during photodynamic therapy: detection by the hypoxia marker EF3  
16 [2-(2-nitroimidazol-1[H]-yl)-N-(3,3,3-trifluoropropyl)acetamide ] *Cancer Res* **60**  
17 2636-42  
18  
19 Carlson D J 2006 Mechanisms of Intrinsic Radiation Sensitivity: The Effects of DNA  
20 Damage Repair, Oxygen, and Radiation Quality In *School of Health Sciences Purdue*  
21 *University: West Lafayette, IN, USA*  
22  
23 Carp S A, Roche-Labarbe N, Franceschini M A, Srinivasan V J, Sakadzic S and Boas D A  
24 2011 Due to intravascular multiple sequential scattering, Diffuse Correlation  
25 Spectroscopy of tissue primarily measures relative red blood cell motion within  
26 vessels *Biomed. Opt. Express* **2** 2047-54  
27  
28 Cheng R 2013 Noninvasive near-infrared diffuse optical monitoring of cerebral  
29 hemodynamics and autoregulation University of Kentucky: Lexington, Kentucky,  
30 USA pp 1-121  
31  
32 Cheng R, Shang Y, Hayes D, Saha S P and Yu G 2012 Noninvasive optical evaluation of  
33 spontaneous low frequency oscillations in cerebral hemodynamics *Neuroimage* **62**  
34 1445-54  
35  
36 Cheng R, Shang Y, Wang S Q, Evans J M, Rayapati A, Randall D C and Yu G 2014  
37 Near-infrared diffuse optical monitoring of cerebral blood flow and oxygenation for  
38 the prediction of vasovagal syncope *J. Biomed. Opt.* **19** 017001  
39  
40 Cheung C, Culver J P, Takahashi K, Greenberg J H and Yodh A G 2001 In vivo  
41 cerebrovascular measurement combining diffuse near-infrared absorption and  
42 correlation spectroscopies *Phys. Med. Biol.* **46** 2053-65  
43  
44 Choe R 2005 Diffuse Optical Tomography and Spectroscopy of Breast Cancer and Fetal  
45 Brain University of Pennsylvania: Philadelphia, USA pp 1-226  
46  
47 Choe R, Putt M E, Carlile P M, Durduran T, Giammarco J M, Busch D R, Jung K W,  
48 Czerniecki B J, Tchou J, Feldman M D, Mies C, Rosen M A, Schnall M D,  
49 DeMichele A and Yodh A G 2014 Optically Measured Microvascular Blood Flow  
50 Contrast of Malignant Breast Tumors *Plos One* **9** e99683  
51  
52 Chung S H, Feldman M D, Martinez D, Kim H, Putt M E, Busch D R, Tchou J, Czerniecki B  
53 J, Schnall M D, Rosen M A, DeMichele A, Yodh A G and Choe R 2015 Macroscopic  
54 optical physiological parameters correlate with microscopic proliferation and vessel  
55 area breast cancer signatures *Breast Cancer Res* **17** 72  
56  
57 Cordero M D, De Miguel M, Fernandez A M M, Lopez I M C, Maraver J G, Cotan D,  
58 Izquierdo L G, Bonal P, Campa F, Bullon P, Navas P and Alcazar J A S 2010  
59 Mitochondrial dysfunction and mitophagy activation in blood mononuclear cells of  
60

- 1  
2  
3 fibromyalgia patients: implications in the pathogenesis of the disease *Arthritis. Res.*  
4 *Ther* **12** R17
- 5  
6 Culver J P, Durduran T, Furuya T, Cheung C, Greenberg J H and Yodh A G 2003 Diffuse  
7 optical tomography of cerebral blood flow, oxygenation, and metabolism in rat during  
8 focal ischemia *J. Cereb. Blood Flow Metab.* **23** 911-24
- 9  
10 Dehaes M, Aggarwal A, Lin P Y, Fortuno C R, Fenoglio A, Roche-Labarbe N, Soul J S,  
11 Franceschini M A and Grant P E 2014 Cerebral oxygen metabolism in neonatal  
12 hypoxic ischemic encephalopathy during and after therapeutic hypothermia *J. Cereb.*  
13 *Blood Flow Metab.* **34** 87-94
- 14  
15 Dehaes M, Cheng H H, Buckley E M, Lin P Y, Ferradal S L, Williams K, Vyas R, Hagan K,  
16 Wigmore D, McDavitt E, Soul J S, Franceschini M A, Newburger J W and Grant P E  
17 2015 Perioperative cerebral hemodynamics and oxygen metabolism in neonates with  
18 single-ventricle physiology *Biomed. Opt. Express* **6** 4749-67
- 19  
20 Dehghani H, Eames M E, Yalavarthy P K, Davis S C, Srinivasan S, Carpenter C M, Pogue B  
21 W and Paulsen K D 2009 Near infrared optical tomography using NIRFAST:  
22 Algorithm for numerical model and image reconstruction *Commun Numer Meth En*  
23 **25** 711-32
- 24  
25  
26 Dietsche G, Ninck M, Ortolof C, Li J, Jaillon F and Gisler T 2007 Fiber-based multispeckle  
27 detection for time-resolved diffusing-wave spectroscopy: characterization and  
28 application to blood flow detection in deep tissue *Appl. Optics* **46** 8506-14
- 29  
30 Dong J, Bi R Z, Ho J H, Thong P S P, Soo K C and Lee K 2012a Diffuse correlation  
31 spectroscopy with a fast Fourier transform-based software autocorrelator *J. Biomed.*  
32 *Opt.* **17** 097004
- 33  
34 Dong L 2015 Diffuse optical measurements of head and neck tumor hemodynamics for early  
35 prediction of chemo-radiation therapy outcomes University of Kentucky: Lexington,  
36 Kentucky, USA pp 1-117
- 37  
38 Dong L, Kudrimoti M, Cheng R, Shang Y, Johnson E L, Stevens S D, Shelton B J and Yu G  
39 2012b Noninvasive diffuse optical monitoring of head and neck tumor blood flow  
40 and oxygenation during radiation delivery *Biomed. Opt. Express* **3** 259-72
- 41  
42 Dong L, Kudrimot M, Irwin D, Chen L, Kumar S, Shang Y, Huang C, Johnson E L, Stevens  
43 S D, Shelton B J and Yu G 2016 Diffuse optical measurements of head and neck  
44 tumor hemodynamics for early prediction of chemo-radiation therapy outcomes *J.*  
45 *Biomed. Opt.* **21** 085004
- 46  
47  
48 Durduran T 2004 Non-invasive measurements of tissue hemodynamics with hybrid diffuse  
49 optical methods University of Pennsylvania: Philadelphia, USA pp 1-208
- 50  
51 Durduran T, Choe R, Baker W B and Yodh A G 2010a Diffuse optics for tissue monitoring  
52 and tomography *Rep. Prog. Phys.* **73** 076701
- 53  
54 Durduran T, Choe R, Yu G, Zhou C, Tchou J C, Czerniecki B J and Yodh A G 2005 Diffuse  
55 optical measurement of blood flow in breast tumors *Opt. Lett.* **30** 2915-7
- 56  
57 Durduran T and Yodh A G 2014 Diffuse correlation spectroscopy for non-invasive,  
58 micro-vascular cerebral blood flow measurement *Neuroimage* **85** 51-63
- 59  
60 Durduran T, Yu G, Burnett M G, Detre J A, Greenberg J H, Wang J J, Zhou C and Yodh A G  
2004 Diffuse optical measurement of blood flow, blood oxygenation, and metabolism  
in a human brain during sensorimotor cortex activation *Opt. Lett.* **29** 1766-8

- 1  
2  
3  
4 Durduran T, Zhou C, Edlow B L, Yu G, Choe R, Kim M N, Cucchiara B L, Putt M E, Shah Q,  
5 Kasner S E, Greenberg J H, Yodh A G and Detre J A 2009 Transcranial optical  
6 monitoring of cerebrovascular hemodynamics in acute stroke patients *Opt. Express*  
7 **17** 3884-902
- 8  
9 Durduran T, Zhou C A, Buckley E M, Kim M N, Yu G, Choe R, Gaynor J W, Spray T L,  
10 Durning S M, Mason S E, Montenegro L M, Nicolson S C, Zimmerman R A, Putt M  
11 E, Wang J J, Greenberg J H, Detre J A, Yodh A G and Licht D J 2010b Optical  
12 measurement of cerebral hemodynamics and oxygen metabolism in neonates with  
13 congenital heart defects *J. Biomed. Opt.* **15** 037004
- 14  
15 Eggebrecht A T, Ferradal S L, Robichaux-Viehoever A, Hassanpour M S, Dehghani H,  
16 Snyder A Z, Hershey T and Culver J P 2014 Mapping distributed brain function and  
17 networks with diffuse optical tomography *Nat Photonics* **8** 448-54
- 18  
19 Fantini S, Franceschinifantini M A, Maier J S, Walker S A, Barbieri B and Gratton E 1995  
20 Frequency-Domain Multichannel Optical-Detector for Noninvasive Tissue  
21 Spectroscopy and Oximetry *Optical Engineering* **34** 32-42
- 22  
23 Favilla C G, Mesquita R C, Mullen M, Durduran T, Lu X P, Kim M N, Minkoff D L, Kasner  
24 S E, Greenberg J H, Yodh A G and Detre J A 2014 Optical Bedside Monitoring of  
25 Cerebral Blood Flow in Acute Ischemic Stroke Patients During Head-of-Bed  
26 Manipulation *Stroke* **45** 1269-74
- 27  
28 Ferrari M, Muthalib M and Quaresima V 2011 The use of near-infrared spectroscopy in  
29 understanding skeletal muscle physiology: recent developments *Philosophical*  
30 *Transactions of the Royal Society a-Mathematical Physical and Engineering Sciences*  
31 **369** 4577-90
- 32  
33 Fletcher G C 1976 Dynamic light scattering from collagen solutions. I. Translational diffusion  
34 coefficient and aggregation effects *Biopolymers* **15** 2201-17
- 35  
36 Franceschini M A, Joseph D K, Huppert T J, Diamond S G and Boas D A 2006 Diffuse  
37 optical imaging of the whole head *J. Biomed. Opt.* **11** 054007
- 38  
39 Gagnon L, Desjardins M, Jehanne-Lacasse J, Bherer L and Lesage F 2008 Investigation of  
40 diffuse correlation spectroscopy in multi-layered media including the human head  
41 *Opt. Express* **16** 15514-30
- 42  
43 Ghosh A, Elwell C and Smith M 2012 Cerebral Near-Infrared Spectroscopy in Adults: A  
44 Work in Progress *Anesth Analg* **115** 1373-83
- 45  
46 Grassi W, Core P, Carlino G, Salaffi F and Cervini C 1994 Capillary-Permeability in  
47 Fibromyalgia *Journal of Rheumatology* **21** 1328-31
- 48  
49 Gurley K 2012 Use of hybrid diffuse optical spectroscopies in continuous monitoring of  
50 blood flow, blood oxygenation and oxygen consumption rate in exercising skeletal  
51 muscle University of Kentucky: Lexington, Kentucky, USA pp 1-81
- 52  
53 Gurley K, Shang Y and Yu G 2012 Noninvasive optical quantification of absolute blood flow,  
54 blood oxygenation, and oxygen consumption rate in exercising skeletal muscle *J.*  
55 *Biomed. Opt.* **17** 075010
- 56  
57 He L 2015 Noncontact diffuse correlation tomography of breast tumor University of  
58 Kentucky: Lexington, Kentucky, USA pp 1-126
- 59  
60 He L, Lin Y, Huang C, Irwin D, Szabunio M M and Yu G 2015 Noncontact diffuse  
correlation tomography of human breast tumor *J. Biomed. Opt.* **20** 86003

- 1  
2  
3 Henry B, Zhao M J, Shang Y, Uhl T, Thomas D T, Xenos E S, Saha S P and Yu G 2015  
4 Hybrid diffuse optical techniques for continuous hemodynamic measurement in  
5 gastrocnemius during plantar flexion exercise *J. Biomed. Opt.* **20** 125006  
6  
7 Hou Y, Shang Y, Cheng R, Zhao Y, Qin Y, Kryscio R, Rayapati A, Hayes D and Yu G 2014  
8 Obstructive sleep apnea-hypopnea results in significant variations in cerebral  
9 hemodynamics detected by diffuse optical spectroscopies *Physiol. Meas.* **35** 2135-48  
10  
11 Huang C, Irwin D, Lin Y, Shang Y, He L, Kong W K, Luo J and Yu G 2015a Speckle  
12 contrast diffuse correlation tomography of complex turbid medium flow *Med Phys* **42**  
13 4000-6  
14  
15 Huang C, Lin Y, He L, Irwin D, Szabunio M M and Yu G 2015b Alignment of sources and  
16 detectors on breast surface for noncontact diffuse correlation tomography of breast  
17 tumors *Appl. Optics* **54** 8808-16  
18  
19 Huang C, Radabaugh J P, Aouad R K, Lin Y, Gal T J, Patel A B, Valentino J, Shang Y and  
20 Yu G 2015c Noncontact diffuse optical assessment of blood flow changes in head and  
21 neck free tissue transfer flaps *J. Biomed. Opt.* **20** 075008  
22  
23 Huang C, Seong M, Morgan J P, Mazdeyasna S, Kim J G, Hastings J T and Yu G 2016 A  
24 low-cost compact diffuse speckle contrast flowmeter using small laser diode and bare  
25 charge-coupled-device *J. Biomed. Opt.* **21** 080501  
26  
27 Intes X, Chen J, Venugopal V and Lesage F 2010 Time-resolved diffuse optical tomography  
28 with patterned-light illumination and detection *Opt. Lett.* **35** 2121-3  
29  
30 Irwin D 2011 Influence of tissue absorption and scattering on diffuse correlation spectroscopy  
31 blood flow measurement University of Kentucky: Lexington, Kentucky, USA pp  
32 1-68  
33  
34 Irwin D, Dong L, Shang Y, Cheng R, Kudrimoti M, Stevens S D and Yu G 2011 Influences  
35 of tissue absorption and scattering on diffuse correlation spectroscopy blood flow  
36 measurements *Biomed. Opt. Express* **2** 1969-85  
37  
38 Jaillon F, Li J, Dietsche G, Elbert T and Gisler T 2007 Activity of the human visual cortex  
39 measured non-invasively by diffusing-wave spectroscopy *Opt. Express* **15** 6643-50  
40  
41 Jaillon F, Skipetrov S E, Li J, Dietsche G, Maret G and Gisler T 2006 Diffusing-wave  
42 spectroscopy from head-like tissue phantoms: influence of a non-scattering layer *Opt.*  
43 *Express* **14** 10181-94  
44  
45 Jermyn M, Ghadyani H, Mastanduno M A, Turner W, Davis S C, Dehghani H and Pogue B  
46 W 2013 Fast segmentation and high-quality three-dimensional volume mesh creation  
47 from medical images for diffuse optical tomography *J. Biomed. Opt.* **18** 86007  
48  
49 Jobsis F F 1977 Noninvasive, infrared monitoring of cerebral and myocardial oxygen  
50 sufficiency and circulatory parameters *Science* **198** 1264-7  
51  
52 Kasikcioglu E, Dinler M and Berker E 2006 Reduced tolerance of exercise in fibromyalgia  
53 may be a consequence of impaired microcirculation initiated by deficient action of  
54 nitric oxide *Medical Hypotheses* **66** 950-2  
55  
56 Kim J G, Xia M N and Liu H L 2005 Extinction coefficients of hemoglobin for near-infrared  
57 spectroscopy of tissue *IEEE Eng. Med. Biol. Mag.* **24** 118-21  
58  
59 Kim M N, Durduran T, Frangos S, Edlow B L, Buckley E M, Moss H E, Zhou C, Yu G, Choe  
60 R, Maloney-Wilensky E, Wolf R L, Grady M S, Greenberg J H, Levine J M, Yodh A  
G, Detre J A and Kofke W A 2010 Noninvasive measurement of cerebral blood flow

- 1  
2  
3 and blood oxygenation using near-infrared and diffuse correlation spectroscopies in  
4 critically brain-Injured adults *Neurocrit. Care* **12** 173-80
- 5  
6 Kim M N, Edlow B L, Durduran T, Frangos S, Mesquita R C, Levine J M, Greenberg J H,  
7 Yodh A G and Detre J A 2014 Continuous Optical Monitoring of Cerebral  
8 Hemodynamics During Head-of-Bed Manipulation in Brain-Injured Adults *Neurocrit.*  
9 *Care* **20** 443-53
- 10  
11 Li J, Dietsche G, Iftime D, Skipetrov S E, Maret G, Elbert T, Rockstroh B and Gisler T 2005  
12 Noninvasive detection of functional brain activity with near-infrared diffusing-wave  
13 spectroscopy *J. Biomed. Opt.* **10** 44002
- 14  
15 Li T, Lin Y, Shang Y, He L, Huang C, Szabunio M and Yu G 2013 Simultaneous  
16 measurement of deep tissue blood flow and oxygenation using noncontact diffuse  
17 correlation spectroscopy flow-oximeter *Sci. Rep.* **3** 1358
- 18  
19 Lin P Y, Hagan K, Fenoglio A, Grant P E and Franceschini M A 2016 Reduced cerebral  
20 blood flow and oxygen metabolism in extremely preterm neonates with low-grade  
21 germinal matrix-intraventricular hemorrhage *Sci. Rep.* **6** 25903
- 22  
23 Lin Y, He L, Shang Y and Yu G 2012 Noncontact diffuse correlation spectroscopy for  
24 noninvasive deep tissue blood flow measurement *J. Biomed. Opt.* **17** 010502
- 25  
26 Lin Y, Huang C, Irwin D, He L, Shang Y and Yu G 2014 Three-dimensional flow contrast  
27 imaging of deep tissue using noncontact diffuse correlation tomography *Applied*  
28 *Physics Letters* **104** 121103
- 29  
30 Lindh M, Johansson G, Hedberg M, Henning G B and Grimby G 1995 Muscle-Fiber  
31 Characteristics, Capillaries and Enzymes in Patients with Fibromyalgia and Controls  
32 *Scandinavian Journal of Rheumatology* **24** 34-7
- 33  
34 Liu H, Boas D A, Zhang Y, Yodh A G and Chance B 1995 Determination of optical  
35 properties and blood oxygenation in tissue using continuous NIR light *Phys Med Biol*  
36 **40** 1983-93
- 37  
38 Maret G and Wolf P E 1987 Multiple Light-Scattering from Disordered Media - the Effect of  
39 Brownian-Motion of Scatterers *Zeitschrift Fur Physik B-Condensed Matter* **65** 409-13
- 40  
41 Maret G and Wolf P E 1989 Multiple Light-Scattering - Weak Localization and Dynamic  
42 Fluctuations *Physica Scripta* **T29** 223-5
- 43  
44 McIver K L, Evans C, Kraus R M, Ispas L, Sciotti V M and Hickner R C 2006 NO-mediated  
45 alterations in skeletal muscle nutritive blood flow and lactate metabolism in  
46 fibromyalgia *Pain* **120** 161-9
- 47  
48 Mesquita R C, Durduran T, Yu G, Buckley E M, Kim M N, Zhou C, Choe R, Sunar U and  
49 Yodh A G 2011 Direct measurement of tissue blood flow and metabolism with  
50 diffuse optics *Philosophical Transactions of the Royal Society a-Mathematical*  
51 *Physical and Engineering Sciences* **369** 4390-406
- 52  
53 Mesquita R C, Putt M, Chandra M, Yu G, Xing X M, Han S W, Lech G, Shang Y, Durduran  
54 T, Zhou C, Yodh A G and Mohler E R 2013 Diffuse optical characterization of an  
55 exercising patient group with peripheral artery disease *J. Biomed. Opt.* **18** 57007
- 56  
57 Morf S, Amann-Vesti B, Forster A, Franzeck U K, Koppensteiner R, Uebelhart D and Sprott  
58 H 2005 Microcirculation abnormalities in patients with fibromyalgia - measured by  
59 capillary microscopy and laser fluxmetry *Arthritis. Res. Ther* **7** R209-R16
- 60  
Munk N, Symons B, Shang Y, Cheng R and Yu G 2012 Noninvasively measuring the

- 1  
2  
3 hemodynamic effects of massage on skeletal muscle: A novel hybrid near-infrared  
4 diffuse optical instrument *Journal of Bodywork and Movement Therapies* **16** 22-8
- 5  
6 Murkin J M and Arango M 2009 Near-infrared spectroscopy as an index of brain and tissue  
7 oxygenation *British Journal of Anaesthesia* **103 (BJA/PGA Supplement)** i3-i13
- 8  
9 Patterson M S, Chance B and Wilson B C 1989 Time resolved reflectance and transmittance  
10 for the non-invasive measurement of tissue optical properties *Appl Opt* **28** 2331-6
- 11  
12 Pine D J, Weitz D A, Chaikin P M and Herbolzheimer E 1988 Diffusing-Wave Spectroscopy  
13 *Phys. Rev. Lett.* **60** 1134-7
- 14  
15 Pine D J, Weitz D A, Zhu J X and Herbolzheimer E 1990 Diffusing-Wave Spectroscopy -  
16 Dynamic Light-Scattering in the Multiple-Scattering Limit *Journal De Physique* **51**  
17 2101-27
- 18  
19 Quaresima V, Ferrari M, Franceschini M A, Hoimes M L and Fantini S 2004 Spatial  
20 distribution of vastus lateralis blood flow and oxyhemoglobin saturation measured at  
21 the end of isometric quadriceps contraction by multichannel near-infrared  
22 spectroscopy *J. Biomed. Opt.* **9** 413-20
- 23  
24 Rice S O 1954 Mathematical analysis of random noise In *Noise and Stochastic Processes*  
25 Wax N ed Dover: New York p 133
- 26  
27 Roche-Labarbe N, Carp S A, Surova A, Patel M, Boas D A, Grant R E and Franceschini M A  
28 2010 Noninvasive optical measures of CBV, StO(2), CBF Index, and rCMRO(2) in  
29 human premature neonates' brains in the first six weeks of life *Hum. Brain Mapp.* **31**  
30 341-52
- 31  
32 Schachner T, Bonaros N, Bonatti J and Kolbitsch C 2008 Near infrared spectroscopy for  
33 controlling the quality of distal leg perfusion in remote access cardiopulmonary  
34 bypass *Eur J Cardiothorac Surg* **34** 1253-4
- 35  
36 Schweiger M and Arridge S 2014 The Toast plus plus software suite for forward and inverse  
37 modeling in optical tomography *J. Biomed. Opt.* **19**
- 38  
39 Shang Y, Chen L, Toborek M and Yu G 2011a Diffuse optical monitoring of repeated  
40 cerebral ischemia in mice *Opt. Express* **19** 20301-15
- 41  
42 Shang Y, Cheng R, Dong L, Ryan S J, Saha S P and Yu G 2011b Cerebral monitoring during  
43 carotid endarterectomy using near-infrared diffuse optical spectroscopies and  
44 electroencephalogram *Phys. Med. Biol.* **56** 3015-32
- 45  
46 Shang Y, Gurley K, Symons B, Long D, Srikuea R, Crofford L J, Peterson C A and Yu G  
47 2012 Noninvasive optical characterization of muscle blood flow, oxygenation, and  
48 metabolism in women with fibromyalgia *Arthritis. Res. Ther* **14** R236
- 49  
50 Shang Y and Yu G 2014 A Nth-order linear algorithm for extracting diffuse correlation  
51 spectroscopy blood flow indices in heterogeneous tissues *Applied Physics Letters* **105**
- 52  
53 Shang Y, Zhao Y, Cheng R, Dong L, Irwin D and Yu G 2009 Portable optical tissue flow  
54 oximeter based on diffuse correlation spectroscopy *Opt. Lett.* **34** 3556-8
- 55  
56 Shuler M S, Reisman W M, Whitesides T E, Kinsey T L, Hammerberg E M, Davila M G and  
57 Moore T J 2009 Near-Infrared Spectroscopy in Lower Extremity Trauma *Journal of*  
58 *Bone and Joint Surgery-American Volume* **91A** 1360-8
- 59  
60 Strangman G, Franceschini M A and Boas D A 2003 Factors affecting the accuracy of  
near-infrared spectroscopy concentration calculations for focal changes in  
oxygenation parameters *Neuroimage* **18** 865-79



- 1  
2  
3 Sunar U, Quon H, Durduran T, Zhang J, Du J, Zhou C, Yu G, Choe R, Kilger A, Lustig R,  
4 Loevner L, Nioka S, Chance B and Yodh A G 2006 Noninvasive diffuse optical  
5 measurement of blood flow and blood oxygenation for monitoring radiation therapy  
6 in patients with head and neck tumors: a pilot study *J. Biomed. Opt.* **11** 064021  
7  
8 Vardi M and Nini A 2008 Near-infrared spectroscopy for evaluation of peripheral vascular  
9 disease. A systematic review of literature *Eur. J. Vasc. Endovasc. Surg.* **35** 68-74  
10  
11 Verdecchia K, Diop M, Lee A, Morrison L B, Lee T Y and St Lawrence K 2016 Assessment  
12 of a multi-layered diffuse correlation spectroscopy method for monitoring cerebral  
13 blood flow in adults *Biomed. Opt. Express* **7** 3659-74  
14  
15 Wang D T, Parthasarathy A B, Baker W B, Gannon K, Kavuri V, Ko T, Schenkel S, Li Z, Li  
16 Z R, Mullen M T, Detre J A and Yodh A G 2016 Fast blood flow monitoring in deep  
17 tissues with real-time software correlators *Biomed. Opt. Express* **7** 776-97  
18  
19 Wolf M, Ferrari M and Quaresima V 2007 Progress of near-infrared spectroscopy and  
20 topography for brain and muscle clinical applications *J. Biomed. Opt.* **12** 062104  
21  
22 Wolf M, Franceschini M A, Paunescu L A, Toronov V, Michalos A, Wolf U, Gratton E and  
23 Fantini S 2003 Absolute frequency-domain pulse oximetry of the brain: methodology  
24 and measurements *Adv Exp Med Biol* **530** 61-73  
25  
26 Yu G 2012a Diffuse Correlation Spectroscopy (DCS): A Diagnostic Tool for Assessing  
27 Tissue Blood Flow in Vascular-Related Diseases and Therapies *Current Medical*  
28 *Imaging Reviews* **8** 194-210  
29  
30 Yu G 2012b Near-infrared diffuse correlation spectroscopy (DCS) for assessing deep tissue  
31 blood flow *Anatomy and Physiology* **2** 1000e115  
32  
33 Yu G 2012c Near-infrared diffuse correlation spectroscopy in cancer diagnosis and therapy  
34 monitoring *J. Biomed. Opt.* **17** 010901  
35  
36 Yu G, Durduran T, Lech G, Zhou C, Chance B, Mohler E R and Yodh A G 2005a  
37 Time-dependent blood flow and oxygenation in human skeletal muscles measured  
38 with noninvasive near-infrared diffuse optical spectroscopies *J. Biomed. Opt.* **10**  
39 024027  
40  
41 Yu G, Durduran T, Zhou C, Wang H W, Putt M E, Saunders H M, Sehgal C M, Glatstein E,  
42 Yodh A G and Busch T M 2005b Noninvasive monitoring of murine tumor blood  
43 flow during and after photodynamic therapy provides early assessment of therapeutic  
44 efficacy *Clin. Cancer. Res.* **11** 3543-52  
45  
46 Yu G, Floyd T F, Durduran T, Zhou C, Wang J J, Detre J A and Yodh A G 2007 Validation  
47 of diffuse correlation spectroscopy for muscle blood flow with concurrent arterial  
48 spin labeled perfusion MRI *Opt. Express* **15** 1064-75  
49  
50 Yu G, Shang Y, Zhao Y, Cheng R, Dong L and Saha S P 2011 Intraoperative evaluation of  
51 revascularization effect on ischemic muscle hemodynamics using near-infrared  
52 diffuse optical spectroscopies *J. Biomed. Opt.* **16** 027004  
53  
54 Zhang W, Gao F, Wu L H, Ma W J, Lu Y M and Zhao H J 2013 A time-domain diffuse  
55 fluorescence and optical tomography system for breast tumor diagnosis *J Infrared*  
56 *Millim W* **32** 181-6  
57  
58 Zhou C 2007 In-Vivo Optical Imaging and Spectroscopy of Cerebral Hemodynamics  
59 University of Pennsylvania: Philadelphia, USA pp 1-325  
60  
Zhou C, Choe R, Shah N, Durduran T, Yu G, Durkin A, Hsiang D, Mehta R, Butler J, Cerussi

1  
2  
3 A, Tromberg B J and Yodh A G 2007 Diffuse optical monitoring of blood flow and  
4 oxygenation in human breast cancer during early stages of neoadjuvant chemotherapy  
5 *J. Biomed. Opt.* **12** 051903  
6

7 Zhou C, Eucker S A, Durduran T, Yu G, Ralston J, Friess S H, Ichord R N, Margulies S S and  
8 Yodh A G 2009 Diffuse optical monitoring of hemodynamic changes in piglet brain  
9 with closed head injury *J. Biomed. Opt.* **14** 034015  
10

11 Zhou C, Yu G, Furuya D, Greenberg J H, Yodh A G and Durduran T 2006 Diffuse optical  
12 correlation tomography of cerebral blood flow during cortical spreading depression in  
13 rat brain *Opt. Express* **14** 1125-44  
14

15 Zirak P, Delgado-Mederos R, Dinia L, Carrera D, Marti-Fabregas J and Durduran T 2014  
16 Transcranial diffuse optical monitoring of microvascular cerebral hemodynamics  
17 after thrombolysis in ischemic stroke *J. Biomed. Opt.* **19** 18002  
18  
19  
20  
21  
22  
23  
24  
25  
26  
27  
28  
29  
30  
31  
32  
33  
34  
35  
36  
37  
38  
39  
40  
41  
42  
43  
44  
45  
46  
47  
48  
49  
50  
51  
52  
53  
54  
55  
56  
57  
58  
59  
60

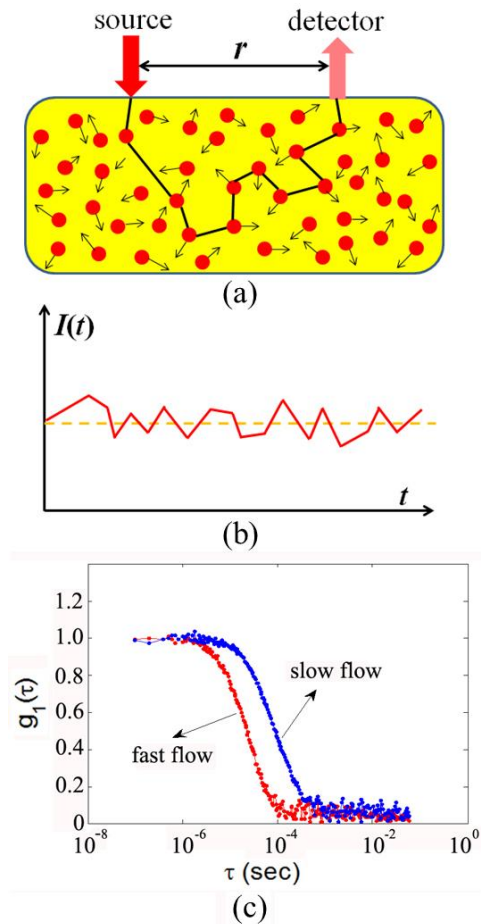
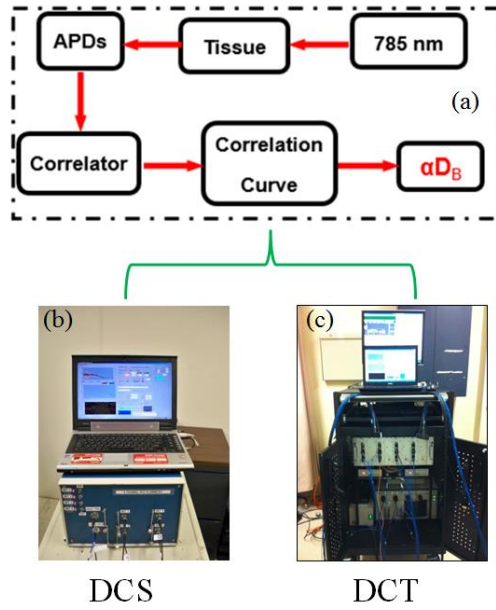


**Fig. 1:** The principle of diffuse correlation spectroscopy (DCS) for blood flow measurements in deep/thick tissues. (a) Source and detector fibers are placed on the tissue surface within a distance of  $r$  for light delivery and collection; (b) Light intensity  $I(t)$ , detected by the APD, fluctuates with time due to the motions of RBCs; (c) Blood flow change can be quantified from the shift of temporal electric field autocorrelation function curves.



25  
26  
27  
28  
29  
30  
31  
32  
33  
34  
35  
36  
37  
38  
39  
40  
41  
42  
43  
44  
45  
46  
47  
48  
49  
50  
51  
52  
53  
54  
55  
56  
57  
58  
59  
60

**Fig. 2:** The schematic diagram (a) and instrument photos of typical DCS (b) and DCT (c) systems.

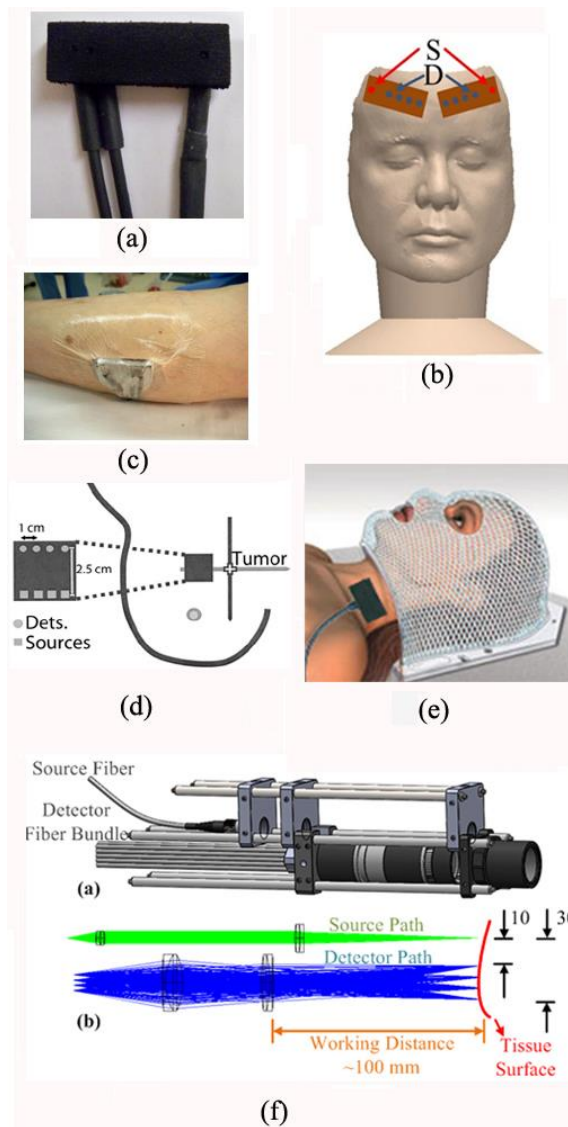


**Fig. 3:** A variety of optical probes for DCS/DCT measurements. (a) A typical DCS probe consisting of source and detector fibers; (b) Two DCS probes taped on both sides of a frontal head for cerebral blood flow measurements; (c) A DCS probe taped on top of the calf muscle; (d) A hand-held DCS probe scanning over a breast tumor; (e) A DCS probe placed on top of the head/neck tumor; (f) A noncontact DCS probe with lens system focusing the source and detectors on the surface of tissue. Some of the figures are reproduced from the subfigures in the references (Huang *et al.*, 2015c; Durduran *et al.*, 2005)

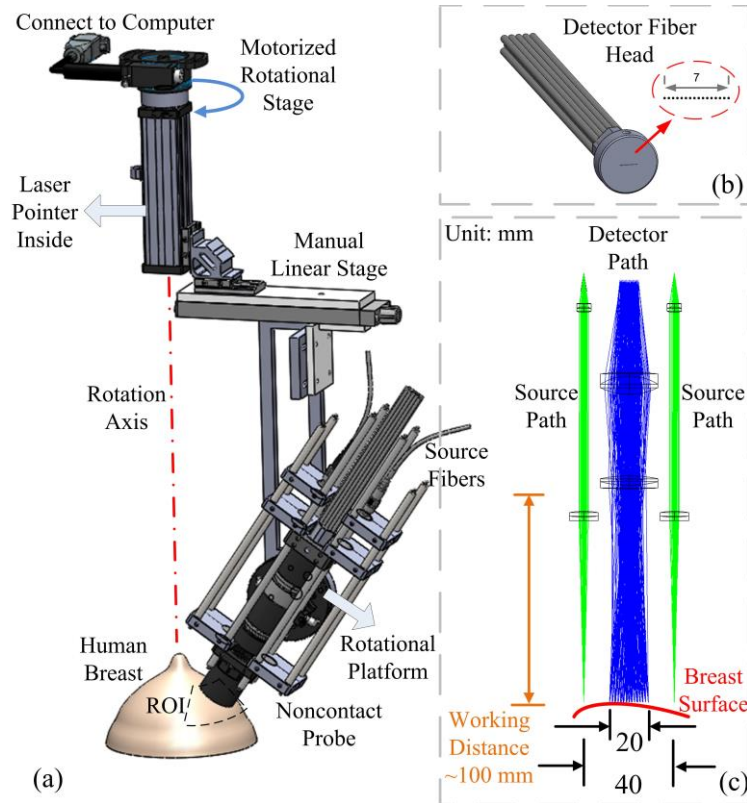


**Fig. 4:** A noncontact DCT probe with rotational scanning system. (a) Noncontact DCT probe head was scanned over a region of interest (ROI) on the breast by a motorized rotational stage, (b) A linear array of single-mode detector fibers, (c) Source and detector fibers were projected on the breast surface using achromatic lenses; two source paths were attached to the sides of the detector path. This figure is reproduced from Fig. 1 in the reference (Huang *et al.*, 2015b).

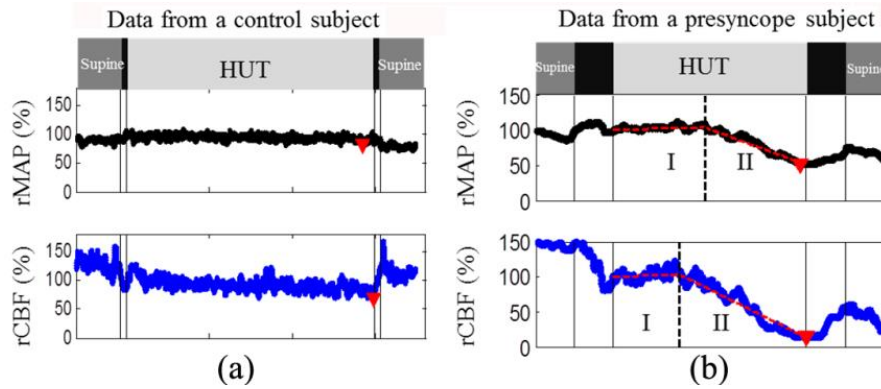


**Fig. 5.** Relative changes in mean artery blood pressure (rMAP) and cerebral blood flow (rCBF) from a control subject **(a)** and a presyncope subject **(b)** during Head-Up-Tilting (HUT). The solid vertical lines indicate the beginning or ending of tilting up and tilting down. The triangles indicate the minima of rMAP and rCBF during HUT. The two connected dashed lines on top of the raw data **(b)** demonstrate the two-line fitting results. The dashed vertical lines indicate the break-points separating Stage I and Stage II. This figure is reproduced from the subfigures of Fig. 1 in the reference (Cheng *et al.*, 2014).

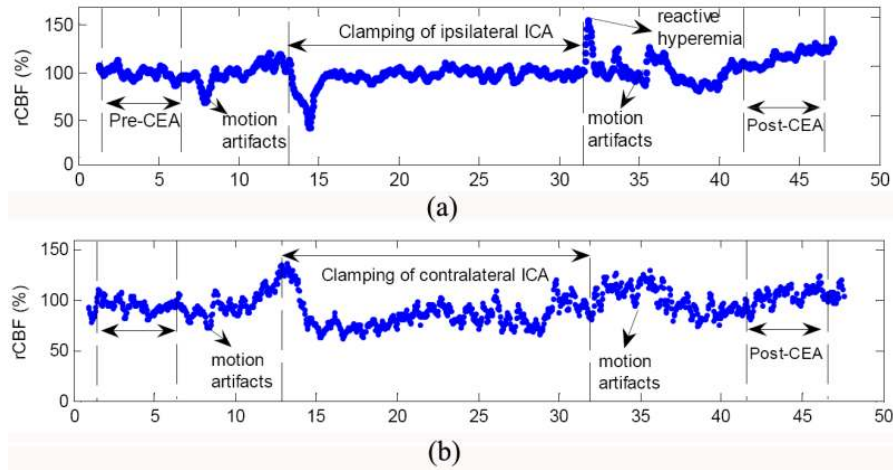


**Fig. 6.** Typical relative changes in cerebral blood flow (rCBF) **(a)** at the surgical side (ipsilateral) and **(b)** at the nonsurgical side (contralateral). This figure is reproduced from subfigures of Fig. 2 in the reference (Shang *et al.*, 2011b).



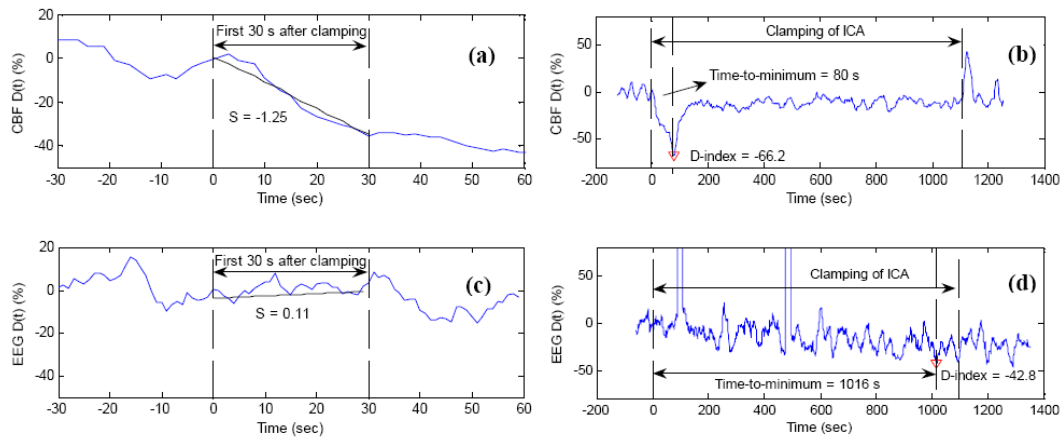


**Fig. 7:** Comparison of DCS and EEG measurement results in a typical patient during carotid endarterectomy (CEA) when the internal carotid artery (ICA) was temporarily clamped. The resulted ischemic status by the ICA clamping was characterized by the slope ( $S$ ),  $D$ -index, and time-to-minimum for both CBF (top panel) and EEG (bottom panel) at the surgical side. Here the slope ( $S$ ) is the decreasing rate of variable  $D(t)$  during the first 30-second clamping period, and  $D(t)$  represents the percentage change of variable (CBF or EEG spectral power) at time  $t$ , when compared to pre-clamping baseline. The minimum of  $D(t)$  during the entire period of clamping is defined as  $D$ -index, representing the most severe cerebral hypoperfusion during ICA clamping. The period from the beginning of clamping to the time of  $D(t)$  attaining its minimum ( $D$ -index) is defined as time-to-minimum. The large negative CBF slope ( $S = -1.25$ ) during the first 30-second clamping period indicates the rapid CBF decrease due to ICA clamping (a). The time duration of CBF decrease and maximal CBF decrease during the entire clamping period were characterized by time-to-minimum (80 s) and  $D$ -index (-66.2%), respectively (b). By contrast, the EEG power changes were small and slow ( $S = 0.11$ ) (c), and reached its minimum ( $D$ -index = -42.8%) in a long period of time (time-to-minimum = 1016 s) (d). This figure is reproduced from Fig. 4 in the reference (Shang *et al.*, 2011b).

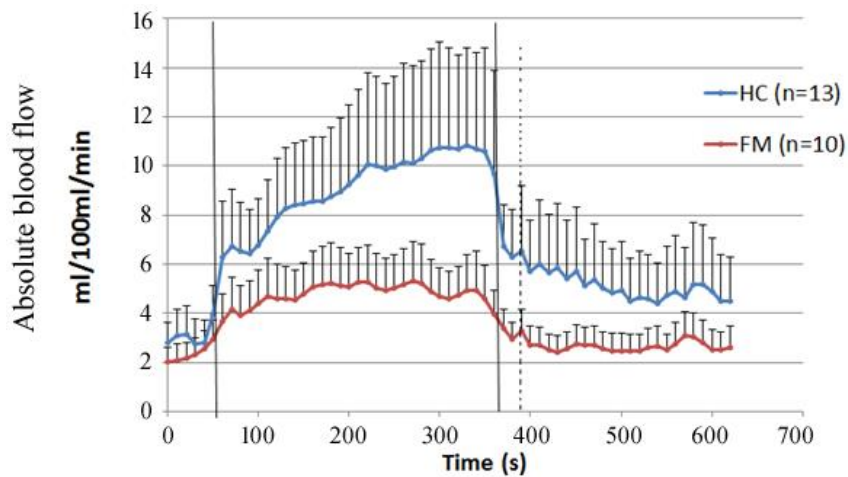


**Fig. 8:** Average absolute blood flow responses to handgrip exercise in 10 subjects with fibromyalgia (FM) and 13 age-matched healthy controls (HC). The vertical lines indicate the beginning and end of exercise. Average pre-exercise blood flow value, determined as the average of data points 30 s before the onset of exercise, was  $3.19 \pm 1.03$  ml/100 ml/min for the healthy subjects and  $2.63 \pm 0.71$  ml/100 ml/min for the FM subjects ( $p = 0.444$ ). Plateau blood flow value, determined as the average of points 30 s before the end of exercise was  $10.71 \pm 3.91$  ml/100 ml/min for healthy subjects and  $4.83 \pm 1.42$  ml/100 ml/min for FM subjects ( $p = 0.018$ ).

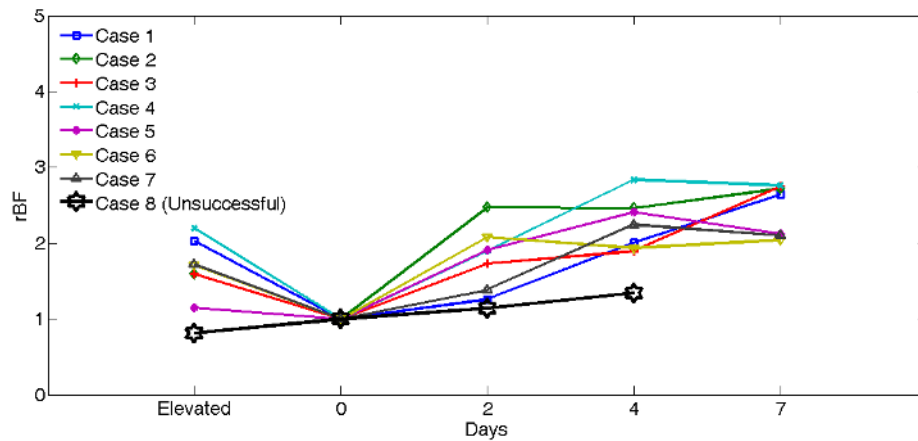


**Fig. 9:** Comparison of rBF changes between seven successful and one unsuccessful flaps. The rBF values over the seven successful cases (Cases 1 to 8) during operation and on postoperative days 2, 4, 7 are presented individually. rBF from the unsuccessful flap case (Case 8) was measured at the time of flap elevation and on postoperative days 2 and 4. The data from the unsuccessful case (Case 8) at Day 7 are not available due to the subsequent re-flap before that day. This figure is reproduced from Fig. 6 in the reference (Huang *et al.*, 2015c).

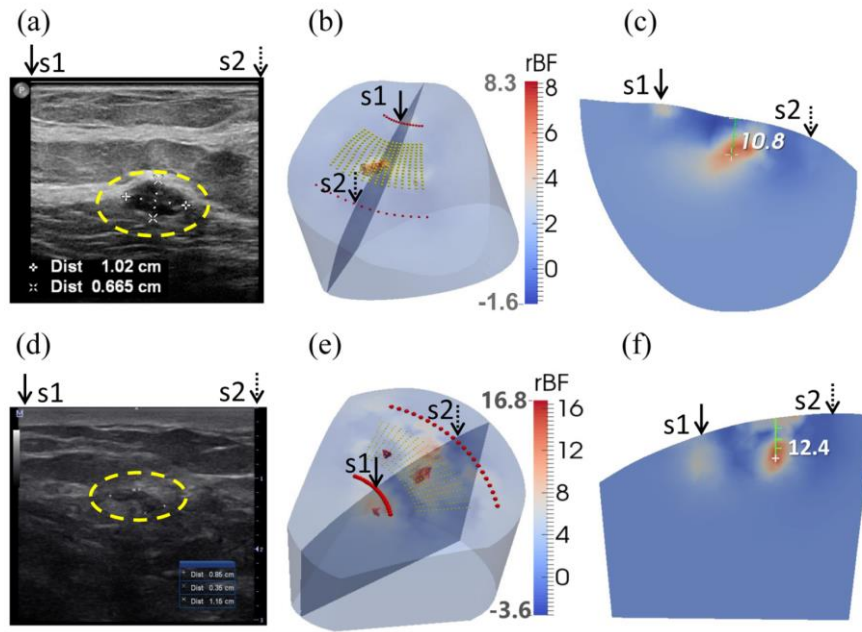


**Fig. 10:** Clinical examples of two low-grade carcinomas in situ. (a) Ultrasound image of breast with a tumor (inside the yellow dashed circle) in the first patient. The tumor mass center is located at 19.2 mm beneath the skin surface. (d) Ultrasound image of breast with a tumor (inside the yellow dashed circle) in the second patient. The tumor mass center is located at 13.3 mm beneath the skin surface. (b) and (e) show the reconstructed 3-D tumor blood flow contrasts imaged by the ncDCT in the first and second patients, respectively. For the comparison of ultrasound and ncDCT results, an ultrasound imaging plane along the transducer line and across the overlapped two specific light sources (S1 and S2) of ncDCT (see Fig. 4) is presented in the 3-D reconstructed image. The backgrounds are presented with 30% transparency of the original color clarity. (c) and (f) show the cross-section views through the reconstructed tumor centers, which can be directly compared to the 2-D ultrasound tumor images [(a) and (d)], respectively. This figure is reproduced from Fig. 8 in the reference (He *et al.*, 2015).

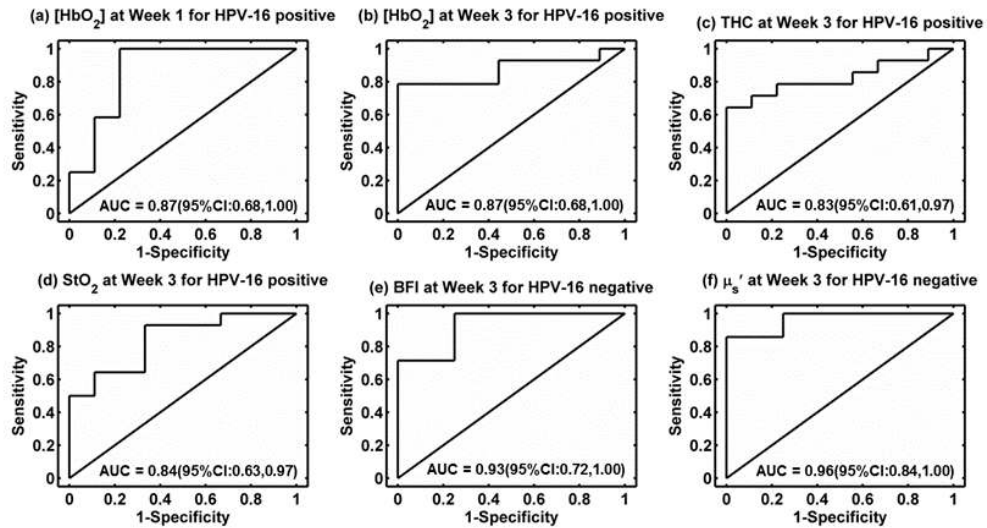


**Fig. 11:** Receiver operating characteristic curves (ROC) and the associated areas under the curve (AUC) for discriminating tumors with incomplete response (IR) or complete response (CR). (a, b) [HbO<sub>2</sub>] at Week 1 and Week 3 in HPV-16 positive patients, (c) THC at Week 3 in HPV-16 positive patients, (d) StO<sub>2</sub> at Week 3 in HPV-16 positive patients, (e) BFI in HPV-16 negative patients at Week 3, and (f)  $\mu_s'$  in HPV-16 negative patients at Week 3. This figure is reproduced from Fig. 5 in the reference (Dong *et al.*, 2016).